Inferring the ice sheet sliding law from seismic observations: A Pine Island Glacier case study

Kevin Hank[1], Robert J. Arthern[1], C. Rosie Williams[1], Alex M. Brisbourne[1], Andrew M. Smith[1], James A. Smith[1], Anna Wåhlin[2], and Sridhar Anandakrishnan[3]

[1]Natural Environment Research Council, British Antarctic Survey, High Cross, Madingley Road, Cambridge, CB3 0ET, United Kingdom
[2]Department of Marine Sciences, University of Gothenburg, Gothenburg, Sweden
[3]Department of Geoscience, Pennsylvania State University, University Park, Pennsylvania, 16802, USA
[*]kevhan@bas.ac.uk

Correspondence: Kevin Hank (kevhan@bas.ac.uk)

Abstract. The response of the Antarctic ice sheet to climate change and its contribution to sea level under different emission scenarios are subject to large uncertainties. A key uncertainty is the slipperiness at the ice sheet base and how it is parameterized in glaciological projections. Alternative formulations of the sliding law exist, but very limited access to the ice base makes it difficult to validate them. Here, the Viscous Grain-Shearing (VGS) theory of acoustic propagation in granular material, together with independent estimates of grain diameter and porosity from sediment cores, is used to relate the effective pressure, which is a key control of basal sliding, to seismic observations recovered from Pine Island Glacier, Antarctica. With basal shear stress and sliding speed derived through satellite observations of ice flow and inverse methods, the new Bayesian sliding law inference – VGS (BASLI–VGS) approach enables a comparison of basal sliding laws within a Bayesian model selection framework. The presented direct link between seismic observations and sliding law parameters can be readily applied to any acoustic impedance data collected in glacial environments underlain by granular material. For rapidly sliding tributaries of Pine Island Glacier, these calculations provide support for a Coulomb-type sliding law and widespread low effective pressures.

1 Introduction

Large uncertainties accompany sea level rise projections for the 21st century. Relative to 1900, the estimates vary between ~ 50 and $> 100 \, \mathrm{cm}$ (IPCC Core Writing Team, H. Lee and J. Romero (eds.), 2023). This uncertainty hampers the formulation of adaptation strategies. A key source of uncertainty is the slipperiness of the bed beneath regions of fast-flowing ice streams (Ritz et al., 2015; Brondex et al., 2017), particularly in the Amundsen Sea Embayment (e.g., Nias et al., 2018; Joughin et al., 2019; Brondex et al., 2019). Despite over 60 years of research on basal sliding (e.g., Weertman, 1957; Lliboutry, 1958a, b, 1959; Budd et al., 1979; Iken, 1981; Iverson et al., 1998; Tulaczyk et al., 2000; Schoof, 2005; Gagliardini et al., 2007; Tsai et al.,

20 2015; Brondex et al., 2017; Zoet and Iverson, 2020), the sliding law operating on large scales in Antarctica remains a matter
of debate.

For ice that slides over the bed, a no-slip boundary condition is inappropriate. Free slip is also unrealistic because basal drag
provides significant resistance to sliding wherever the ice is not floating. Instead, a sliding law that relates basal shear stress
to sliding speed is needed. Alternative formulations of this sliding law have been proposed, applying to different subglacial
25 circumstances (e.g., Fig. 1b-f). The frequently used Weertman-type power law (e.g., Weertman, 1957; Arthern et al., 2015; Ritz
et al., 2015; Arthern and Williams, 2017; Brondex et al., 2017; Kyrke-Smith et al., 2017; Hank and Tarasov, 2024) considers
ice slipping over a rough, hard bed, with ice deforming to pass around large obstacles while bypassing smaller obstacles by
pressure melting and regelation (Fig. 1b; Weertman, 1957). In contrast, Lliboutry envisaged discontinuous ice contact with a
hard bed, separated by water-filled subglacial cavities (Fig. 1c; Lliboutry, 1958a, b, 1959). Later studies show this cavitation
30 could lead to an upper bound for basal shear stress, even for fast-sliding glaciers (Iken, 1981; Schoof, 2005), and the upper
bound was subsequently included in analytically derived sliding laws (Schoof, 2005; Gagliardini et al., 2007).
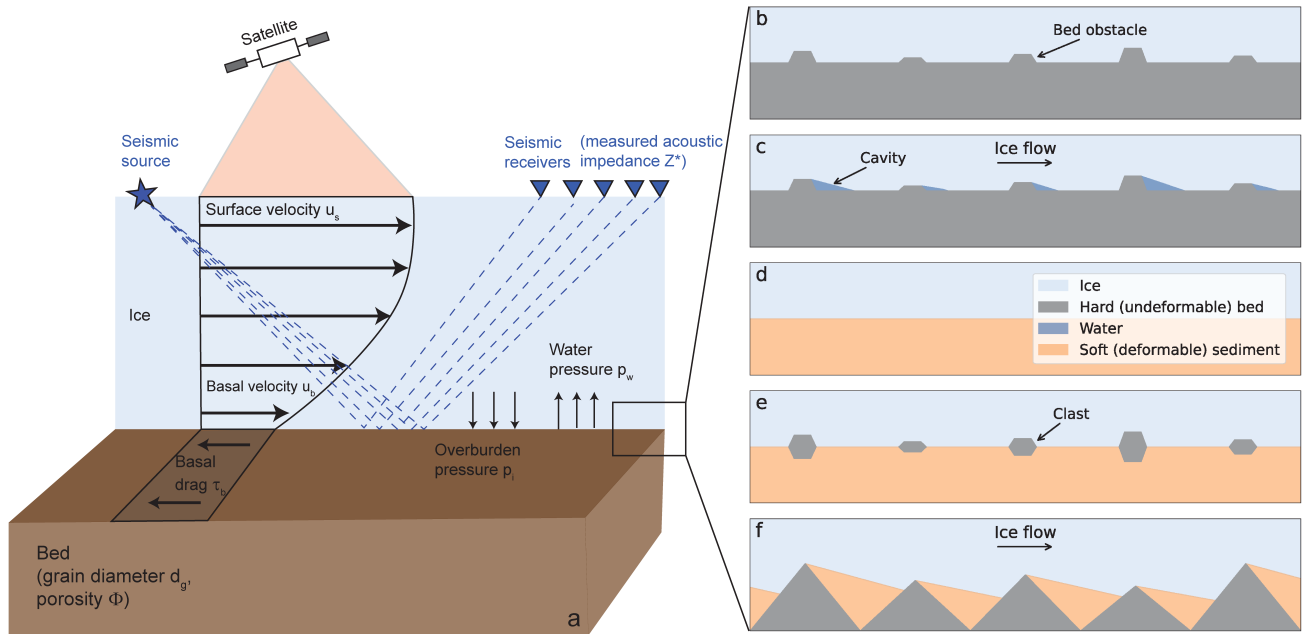
Figure 1. Experimental setup (a) and schematics of the bed considered for different sliding laws (b-f). The schematics are not to scale. Details
of the experimental setup are outlined in Fig. 2 and the text.

Another type of basal drag law is based on sliding lubricated by a deforming layer of sediment that yields, either in a
rate-dependent (viscoplastic) fashion or according to a rate-independent plastic law (Fig. 1d; e.g., Budd et al., 1979; Iverson
et al., 1998; Tulaczyk et al., 2000). One such boundary condition is a Coulomb sliding law, for which the basal shear stress
35 is independent of sliding speed, but varies in proportion to the effective pressure, i.e. the difference between the weight of
the overlying ice and the subglacial water pressure. Higher effective pressures lead to greater compression within the granular

sediment. In an alternative formulation, a modification of the Weertman-type power law that accounts for a strong dependence of the basal shear stress on effective pressure found in laboratory experiments has been proposed (Budd et al., 1979).

Ice loss projections, particularly of the Amundsen Sea Embayment, are sensitive to the applied sliding law, with sliding law parameters being a key source of uncertainty (e.g., Gillet-Chaulet et al., 2016; Brondex et al., 2017; Joughin et al., 2019; Brondex et al., 2019; Barnes and Gudmundsson, 2022). Previous approaches constraining the basal properties, i.e. the sliding law parameters, generally rely on remote sensing data and inverse methods (e.g., Arthern et al., 2015; Hoffman et al., 2018; Gudmundsson et al., 2019; Ranganathan et al., 2021) or seismic observations (e.g., Smith et al., 2013; Brisbourne et al., 2017) but lack a direct link between observations and the representation of basal sliding in ice sheet models (Kyrke-Smith et al., 2017).

Here, we present the new BAyesian Sliding Law Inference – Viscous Grain-Shearing (BASLI–VGS) methodology, which enables the quantitative determination of the most appropriate basal sliding law by directly comparing the measured and predicted acoustic impedance, i.e. the product of the compressional wave speed and density of the subglacial material (Fig. 2). The seismic reflection coefficient from the bed is sensitive to the contrast in acoustic impedance between ice and bed. Because the acoustic impedance of ice is known ($3.33 \pm 0.04 \cdot 10^6$ kg m^{-2} s^{-1}; Atre and Bentley, 1993), this allows the acoustic impedance of the bed to be recovered from seismic reflection surveys performed in the field (Fig. 1a). The VGS theory of acoustic propagation in granular material (Buckingham, 1997, 2000, 2005, 2007) relates the acoustic impedance to the effective pressure, providing a direct link to the basal sliding law: in most laws, low effective pressure, i.e. high basal water pressure, is associated with fast ice sliding over slippery sediment. As basal water pressure has only been measured directly in a few locations via hot-water drilled boreholes (e.g., Engelhardt et al., 1990; Engelhardt and Kamb, 1997; Lüthi et al., 2002; Smith et al., 2021), it has been difficult to map effective pressure. The new approach provides effective pressure over a much wider area.

2   Methods

2.1   Linking seismic observations and basal sliding laws

The sliding laws examined in this study (Sec. 2.2) are thought to represent sliding over different subglacial beds (Fig. 1b-f). To infer which of these sliding laws is most probable, we first derive the basal shear stress (τ_b) and sliding speed (u_b; Fig. 2 and S1) from inverse methods using the Wavelet-based Adaptive-grid Vertically-integrated Ice-sheet-model (WAVI; Arthern et al., 2015; Bradley et al., 2024, Sec. 2.3). The effective pressure (N) can then be estimated by rearranging the sliding laws.

The VGS theory (Sec. 2.4) provides a model of acoustic propagation in granular material. Substituting the estimated effective pressure into this model and using independent estimates for grain diameter (d_g) and porosity (ϕ) from sediment cores (Engelhardt et al., 1990; Stone and Clarke, 1993; Smith et al., 2011; Kirshner et al., 2012; Smith et al., 2014, 2017; Clark et al., 2024, and Smith, unpublished data), provides an estimate of acoustic impedance for each sliding law. The predicted acoustic impedance is then compared to acoustic impedance measurements collected at five sites on Pine Island Glacier (PIG)

in Antarctica (Fig. 4; Brisbourne et al., 2017) by calculating the misfit $\chi^2_{\Theta_i}$ according to

70
$$\chi^2_{\Theta_i} = \frac{1}{N_d} \sum_j^{N_d} \frac{\left(Z_{\Theta_i,j} - Z_j^*\right)^2}{\sigma_j^2}, \tag{1}$$

where $N_d = 300$ is the number of data points (60 per site, 120 m apart), and $Z_{\Theta_i,j}$ are the acoustic impedance predictions under a given sliding law i and the model parameters Θ_i (grain diameter and porosity, along with any additional sliding-law-specific parameters; further details in Sec. 2.2 and 2.5). Data points are treated as independent: a sub-sampled data set (every 10th data point) generally yields the same conclusions (Fig. S2 and S3). While there is evidence that PIG is largely underlain by

75 deformable sediments (Muto et al., 2016; Brisbourne et al., 2017), the exact values of Θ_i are uncertain. Therefore, the misfit $\chi^2_{\Theta_i}$ is systematically assessed across what is considered to be a reasonable parameter space (Sec. 2.5). The model parameters do not vary spatially. Z_j^* and σ_j are the acoustic impedance observations and their uncertainties. As an example, all metrics involved in predicting the acoustic impedance and calculating the misfit $\chi^2_{\Theta_i}$ (u_b, τ_b, N, Z_{Θ_i}, Z^*, σ) are shown for one set of parameter values ($d_g = 0.063$ mm, $\phi = 0.43$, Coulomb friction coefficient $\mu = 0.49$) and the Coulomb sliding law in Fig. S4.
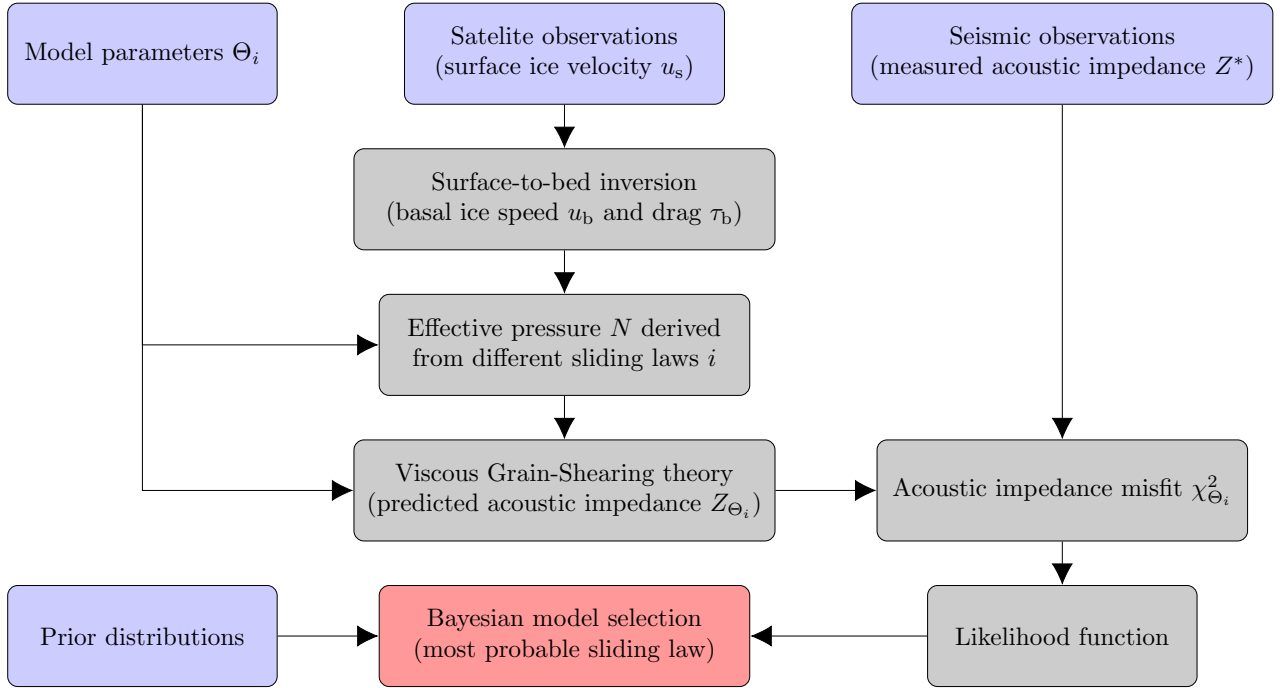
Figure 2. Flowchart of the presented BASLI–VGS methodology. Refer to the text for further details.

80 However, inferring the best-candidate sliding law based solely on the minimum misfit is inadequate, as it does not take into account any prior assessment of the probability of the parameter values used. Instead, we use Bayesian model selection (Sec. 2.5) to identify the most probable sliding law based on all misfits within the parameter space (likelihood function in

Fig. 2). In this framework, the a priori probability of each model, and of particular parameter values within each model, is specified by prior distributions. Using Bayes' rule, these prior probabilities are updated using seismic data, to provide posterior

85   probabilities. Ultimately, this allows us to compute the normalized posterior probability of each sliding law, given the seismic observations collected on PIG (Eq. 20). An advantage of the Bayesian approach is that Occam's razor is automatically applied: overly flexible models with a large range or dimension of parameter space are penalized relative to simpler, less flexible models with fewer parameters or tighter bounds upon parameters.

2.2   Basal sliding laws

90   The effective pressure required as input for the VGS theory is determined based on the basal sliding laws described here. Usually, these laws are expressed so that basal drag is a function of sliding speed and effective pressure. To compute effective pressures, these relationships must be inverted, either by explicitly rearranging the equations or by numerical root-finding. For all sliding laws and sites, we ensure the effective pressure does not exceed the ice overburden pressure.

Strictly speaking, the VGS theory used to predict acoustic impedance only applies to granular material (Sec. 2.4). However,

95   while the formation of cavities, for example, is most appropriate for undeformable bed protrusions, larger rock fragments embedded in granular sediment or even fine-grained deformable sediment might play a similar role (Schoof, 2007a, b; Fowler, 2009; Schoof et al., 2012). Therefore, whenever we are using a sliding law initially developed for hard bedrock (Sec. 2.2.3 and 2.2.6), we assume a granular, relatively undeformable material that can not support tangential friction at its interface with the ice (here referred to as *rigid bed*).

2.2.1   Fixed effective pressure

100

The most straightforward approach for estimating the effective pressure (N) – one that does not require the specification of a sliding law – is to assume it is at a fixed fraction of the ice overburden pressure (p_{i}) everywhere. To contextualize and constrain the results obtained using effective pressures derived from various sliding laws (Sec. 2.2.3 to 2.2.7), we compute the acoustic impedance corresponding to different fractions of the ice overburden pressure, including the two fixed effective

105   pressure endmember scenarios; a lower bound $N = 0\,\mathrm{Pa}$ for which the ice is assumed to be at floatation everywhere, and b) an upper bound, $N = p_{\mathrm{i}}$, for which the effective pressure is assumed equal to the ice overburden pressure everywhere. These endmembers correspond, respectively, to situations where basal water pressure fully supports the weight of overlying ice or does not support any weight at all.

2.2.2   Weertman

110   The Weertman-type power law (Weertman, 1957) assumes that ice slides perfectly over a rigid bed. A thin water film separating the ice and undeformable bed, allows locally for free slip. The basal drag τ_{b} – resistance to basal motion u_{b} – is instead induced by form drag as the ice deforms around the bed obstacles (Fig. 1b). This leads to the relationship

$$\tau_{\mathrm{b}} = C_{\mathrm{W}} u_{\mathrm{b}}^{m}, \tag{2}$$

where C_{W} and $m = 1/3$ are, respectively, the Weertman friction parameter and exponent (often related to the creep exponent n in Glen's flow law, $m = 1/n$). As Eq. 2 does not depend on the effective pressure, the Weertman-type power law can not be directly tested within this approach. Instead, we calculate the acoustic impedance for the Budd sliding law.

2.2.3 Budd

Laboratory experiments examining temperate ice sliding over bed surfaces with a wide range of roughnesses (e.g., Fig. 1b) indicate that τ_{b} exhibits a strong dependence on N (Budd et al., 1979). Consequently, the Weertman-type power law was modified to account for this dependence.

$$\tau_{\mathrm{b}} = C_{\mathrm{B}} u_{\mathrm{b}}^m N^q, \tag{3}$$

where C_{B} and $q = 1$ are the Budd friction parameter and exponent, respectively.

2.2.4 Coulomb

The Coulomb-type plastic rheology sliding law describes ice sliding over soft, deformable sediments (Fig. 1d; Iverson et al., 1998; Tulaczyk et al., 2000).

$$\tau_{\mathrm{b}} = \mu N, \tag{4}$$

where $\mu = \tan(\Phi)$ is the Coulomb friction coefficient and Φ the till friction angle.

2.2.5 Tsai-Budd

A simple sliding law describing basal motion as the combination of ice deformation around and across bed obstacles (Weertman) and deformation of the underlying sediment (Coulomb; Fig. 1e or f; Tsai et al., 2015) takes the form

$$\tau_{\mathrm{b}} = \min[C_{\mathrm{W}} u_{\mathrm{b}}^m, \mu N]. \tag{5}$$

As for the Weertman-type power law itself, Eq. 5 can not be tested in the context discussed here because the Weertman part of the sliding law has no dependence on the effective pressure. To overcome this issue, we replace the Weertman part of Eq. 5 with the Budd sliding law (Eq. 3):

$$\tau_{\mathrm{b}} = \min[C_{\mathrm{B}} u_{\mathrm{b}}^m N^q, \mu N]. \tag{6}$$

2.2.6 Schoof

Eq. 2 and 3 neglect Iken's bound induced by water-filled cavities (upper bound of τ_{b}/N determined by the maximum up-slope angle of the bed in flow direction (β); Fig. 1c; Iken, 1981; Schoof, 2005; Gagliardini et al., 2007). Thus, Schoof (2005) derived a new sliding law incorporating this upper bound. Strictly speaking, the Schoof sliding law only applies to linear ice rheology.

Gagliardini et al. (2007) then numerically extended the relationship to non-linear rheologies. Here we use a generalized form of this sliding law (Brondex et al., 2017):

$$\tau_{\mathrm{b}} = \frac{C_{\mathrm{S}} u_{\mathrm{b}}^m}{(1 + (C_{\mathrm{S}}/(C_{\max} N))^{1/m} u_{\mathrm{b}})^m}, \tag{7}$$

where C_{S} is the Schoof friction parameter and $C_{\max} = \tan\beta$ represents Iken's bound (Iken, 1981; Schoof, 2005).

2.2.7 Zoet-Iverson

Based on experiments in which pressurized ice at its melting temperature is slid over a water-saturated till bed, Zoet and Iverson (2020) derived the following sliding law for glaciers on deformable beds (Fig. 1e):

$$\tau_{\mathrm{b}} = N\mu \left(\frac{u_{\mathrm{b}}}{u_{\mathrm{b}} + u_{\mathrm{t}}} \right)^{\frac{1}{p}}, \tag{8}$$

where the transition speed

$$u_{\mathrm{t}} = \frac{\left(\frac{1}{\eta (Ra)^2 k_0^3} + \frac{4 C_1}{(Ra)^2 k_0} \right) (N_F N)}{(2 + N_F k)}, \tag{9}$$

$k_0 = \frac{2\pi}{4R}$, and the regelation parameter $C_1 = C_p \frac{K}{L}$. Slightly rearranging Eq. 8 and 9 allows us to numerically determine N

$$\tau_{\mathrm{b}} = N\mu \left(\frac{u_{\mathrm{b}}}{u_{\mathrm{b}} + C_{\mathrm{ZI}} N} \right)^{\frac{1}{p}}, \tag{10}$$

where

$$C_{\mathrm{ZI}} = \frac{\left(\frac{1}{\eta (Ra)^2 k_0^3} + \frac{4 C_1}{(Ra)^2 k_0} \right) N_F}{(2 + N_F k)} \tag{11}$$

is the transition speed coefficient (u_{t} without the dependence on N). All other parameters are listed in Table. 1.

While the mathematical form of the Schoof (Eq. 7) and Zoet-Iverson sliding law (Eq. 10) is very similar, the physical reasoning and interpretation differ. The Schoof sliding law is most applicable for ice sliding over a rigid bed (granular but relatively undeformable material), whereas the Zoet-Iverson sliding law aims to describe ice sliding over a water-saturated till bed (deformable). Similarly, the sliding-law-specific parameters μ and $C_{\max}$ represent distinct physical properties, and, may therefore differ significantly (Sec. 2.5).

2.3 Surface-to-bed inversion

Basal shear stress and basal sliding speed are derived using the ice sheet model WAVI, which is vertically integrated but retains an implicit velocity-depth profile (Arthern et al., 2015; Bradley et al., 2024). Data assimilation methods are used to ~~initialise~~ initialize the model into a present-day state (approximately 2015): spatially varying two-dimensional fields of ice stiffness and basal drag are calculated by matching modelled surface velocities with observations of surface velocities (Mouginot et al., 2022), accumulation rates (Arthern et al., 2006), and thinning rates (Smith et al., 2020). Internal ice temperatures are provided

Variable	Description	Value	Unit
p	slip exponent	5	-
η	effective ice viscosity	$3.2 \cdot 10^{12}$	Pa s
R	clast radius	0.015	m
a	fraction of clast radius that protrudes from bed surface	0.25	-
C_p	depression of the melting temperature of ice with pressure	$7.4 \cdot 10^{-8}$	K Pa^{-1}
K	mean thermal conductivity of ice and rock	2.55	W m^{-1} K^{-1}
L	volumetric latent heat of ice	$3 \cdot 10^8$	J m^{-3}
N_f	till bearing capacity factor	33	-
k	till strength reduction resulting from the ice pressure shadow in the lee of clasts	0.1	-

Table 1. Parameters used in Eqs. 10 and 11 (supplementary material of Zoet and Iverson (2020) and references therein).

from a thermal solve of the BISICLES ice sheet model (Cornford et al., 2013). Full details of the inverse method are detailed in Arthern et al. (2015), and the resulting basal sliding speed and basal shear stress are shown in Fig. S1. In this inversion, the basal drag is identified using the Weertman sliding law. However, the sliding relationship that links basal drag and basal speed can be ~~re-parameterised~~ re-parameterized in terms of any of the selected sliding laws that we test here, as long as neither the basal speed nor the basal drag are altered in this process.

2.4 Viscous Grain-Shearing theory

The Viscous Grain-Shearing (VGS) theory (Buckingham, 1997, 2000, 2005, 2007) is used to relate seismic observations to effective pressure (Fig. 2). According to the VGS theory, the elastic deformation under effective pressure that generates frictional resistance also stiffens the sediment and increases the speed of propagation of sound waves. Changes in the speed of sound alter the acoustic impedance ($Z = \rho_s c_p$), the product of the compressional wave speed in the sediment (c_p) and density (ρ_s). In turn, the acoustic impedance controls the reflection coefficient of seismic energy from the base of the ice sheet. The acoustic propagation model predicts the compressional wave speed ($c_p = \psi[N, d_g, \phi, f_s]$) as a function of effective pressure (N), grain diameter (d_g), porosity (ϕ), and seismic frequency (f_s). The link between the compressional wave speed and effective pressure predicted by the acoustic model provides an avenue to test whether a given sliding law applies at any location. All other parameters of the acoustic propagation model have been calibrated using acoustic observations of the ocean floor.

The governing equation for the compressional wave speed is

$$c_p = \frac{c_0}{\mathrm{Re}\left[1 + \zeta \left(i\omega T\right)^q g\left(\omega \tau_p\right)\right]^{-1/2}}, \tag{12}$$

where $c_0 = \sqrt{\frac{\kappa_0}{\rho_0}}$ is the sound speed in the absence of grain-to-grain interactions, $\kappa_0 = \left(\frac{\phi}{\kappa_\mathrm{p}} + \frac{1-\phi}{\kappa_\mathrm{g}}\right)^{-1}$ the bulk modulus of the medium, and $\rho_0 = \phi\rho_\mathrm{p} + (1-\phi)\rho_\mathrm{g}$ the bulk density of the medium. The dimensionless grain-shearing coefficient is

$$\zeta = \frac{\gamma_\mathrm{p} + (4/3)\,\gamma_\mathrm{s}}{\rho_0 c_0^2}, \tag{13}$$

where $\gamma_\mathrm{p} = \gamma_\mathrm{p0}\left[\frac{N d_\mathrm{g}}{N_0 d_\mathrm{g0}}\right]^{1/3}$ and $\gamma_\mathrm{s} = \gamma_\mathrm{s0}\left[\frac{N d_\mathrm{g}}{N_0 d_\mathrm{g0}}\right]^{2/3}$ are the compressional and shear rigidity coefficients, respectively. $N_0 = (1-\phi_0)(\rho_\mathrm{g} - \rho_\mathrm{p})g z_0$ is the reference effective pressure. The function

$$g(\omega\tau_\mathrm{p}) = \left(1 + \frac{1}{i\omega\tau_\mathrm{p}}\right)^{-1+q} \tag{14}$$

accounts for the effect of the viscosity of the molecularly thin layer of pore fluid between contiguous grains (ν). Molecularly thin films become progressively more viscous as they are squeezed, and, therefore, ν differs significantly from the viscosity of the bulk fluid (Israelachvili, 1986; Luengo et al., 1996; Granick, 1999). The compressional viscoelastic time constant τ_p is defined as $\tau_\mathrm{p} = \nu/E$, where E is a spring constant (Buckingham, 2005). The values of τ_p used in the VGS theory are visual fits to the *SAX99* experiments (Buckingham, 2007). However, the measurements were taken in 18 to 19 m deep water (Richardson et al., 2001). Therefore, the exerted overburden pressure is ~ 2 orders of magnitude smaller (less squeezed) than under PIG (ice thickness of 1500 to 2500 m in tributaries, e.g., Fretwell et al., 2013)(ice thickness of 1500 to 2500 m in tributaries; e.g., Fretwell et a. While it is apparent that the viscosity of molecularly thin layers increases with the applied pressure (or loading) p_L, the exact relationship between p_L, the thickness of the thin film, and the viscosity ν is not straightforward (e.g., Israelachvili, 1986; Luengo et al., 1996; Yamada, 2003). Assuming $\nu \propto p_\mathrm{L}$, we set $\tau_\mathrm{p} = 0.012$ s (2 orders of magnitude larger than the value in Buckingham, 2007). However, future studies should further explore the adaptation of the VGS theory from oceanographic to glacial contexts.

$\omega = 2\pi f$ is the angular frequency, $i = \sqrt{-1}$, and Re returns the real part of a complex number. All other parameters are listed in Table 2.

2.5 Bayesian model selection

We compare the different sliding laws using Bayes' Rule:

$$P(M_i|D,I) = \frac{P(D,I|M_i)\,P(M_i)}{P(D,I)}, \tag{15}$$

where D represents the data (acoustic impedance observations), I represents the inverted u_b and τ_b, and M_i represents the model for sliding law i together with the VGS theory. However, the situation here slightly differs from the routine application of Bayes' rule for inferring model parameters within a single model and is more akin to Bayesian model selection. The main difference for the model selection framework is that the probability space is extended to cover multiple models, each of which has its own parameter space. Since the number of parameters differs between models (e.g., two for the fixed effective pressure scenarios and four for the Zoet-Iverson sliding law) and we aim to compare the posterior probabilities of models $P(M_i|D,I)$,

Variable	Description	Value	Unit
T	arbitrary time introduced to avoid awkward dimensions	1	s
q	strain hardening index	0.0851	-
κ_p	bulk modulus of pores	$2.374 \cdot 10^9$	Pa
κ_g	bulk modulus of grains	$3.6 \cdot 10^{10}$	Pa
ρ_P	density of pore fluid	1005	kg m^{-3}
ρ_g	density of grains	2730	kg m^{-3}
γ_p0	reference compressional coefficient	$3.888 \cdot 10^8$	Pa
γ_s0	reference shear coefficient	$4.588 \cdot 10^7$	Pa
d_g0	reference grain diameter	$1 \cdot 10^{-3}$	m
ϕ_0	reference porosity	0.377	-
g	acceleration due to gravity	9.81	m s^{-2}
z_0	reference depth in sediment	0.3	m
f_s	seismic frequency	100	Hz
τ_P	compressional viscoelastic time constant	0.012	s

Table 2. Parameters used in the VGS theory. The values for f_s and τ_P are based on seismic frequencies in a glaciological context and a scaling analysis of the value used in Buckingham (2007), respectively. All other values are adopted from Buckingham (2005).

not the joint posterior probability of models and parameters $P(\Theta_i, M_i | D, I)$, we marginalize over the model parameters Θ_i to retrieve $P(D, I | M_i)$:

$$P(D, I | M_i) = \int_{\Theta_i} P(D, I | \Theta_i, M_i)\, P(\Theta_i | M_i)\, d\Theta_i \tag{16a}$$

$$= \int_{\Theta_i} P(D | I, \Theta_i, M_i)\, P(I | \Theta_i, M_i)\, P(\Theta_i | M_i)\, d\Theta_i. \tag{16b}$$

Assuming the error of the data follows a Gaussian distribution, the likelihood of the acoustic impedance data given the model, its parameters, and the inverted $u_\mathrm{b} - \tau_\mathrm{b}$ is calculated according to

$$P(D | I, \Theta_i, M_i) = \exp\left(-0.5\chi^2_{\Theta_i}\right). \tag{17}$$

Therefore, the posterior probability of each model M_i is

$$P(M_i | D, I) = \frac{\int_{\Theta_i} \exp\left(-0.5\chi^2_{\Theta_i}\right) P(I | \Theta_i, M_i)\, P(\Theta_i | M_i)\, d\Theta_i\, P(M_i)}{\sum_{j=1}^n \int_{\Theta_j} \exp\left(-0.5\chi^2_{\Theta_j}\right) P(I | \Theta_j, M_j)\, P(\Theta_j | M_j)\, d\Theta_j\, P(M_j)}. \tag{18}$$

The prior information from the inverted $u_b - \tau_b$ (not used to constrain $P(\Theta_i|M_i)$) can be directly incorporated into an updated prior using Bayes' rule:

$$P(\Theta_i|I, M_i) = \frac{P(I|\Theta_i, M_i)\, P(\Theta_i|M_i)}{P(I|M_i)}, \tag{19}$$

where $P(I|M_i) = \int_{\Theta_i} P(I|\Theta_i, M_i)\, P(\Theta_i|M_i)\, d\Theta_i$ is a normalization term. Eq. 18 can then be written as

$$P(M_i|D, I) = \frac{\int_{\Theta_i} \exp\left(-0.5\chi^2_{\Theta_i}\right) P(\Theta_i|I, M_i)\, d\Theta_i\, P(M_i|I)}{\sum_{j=1}^{n} \int_{\Theta_j} \exp\left(-0.5\chi^2_{\Theta_j}\right) P(\Theta_j|I, M_j)\, d\Theta_j\, P(M_j|I)}, \tag{20}$$

where we use a prior $P(M_i|I) = 1/n$ that considers each sliding law equally probable, with n being the number of sliding laws considered. Posterior probabilities calculated using $P(M_i) = 1/n$, i.e. without the normalization through $P(I|M_i)$ in Eq. 19, are shown in Fig. S6.

Finally, the prior distributions for all model parameters $P(\Theta_i|M_i)$ need to be defined. The prior distributions for all individual parameters are shown in Fig. 3. The combination of multiple individual priors creates a model's parameter space Θ_i and determines the model prior $P(\Theta_i|M_i)$. Since the parameter space differs between the models (number of individual parameters (dimensions) as well as number of tested parameter values), we ensure $\int_{\Theta_i} P(\Theta_i|M_i)\, d\Theta_i = 1$ for all models. This normalization reflects the fact that once a model has been chosen, the parameters of that model must lie somewhere within its parameter space with certainty. This is self-evident and automatically applies Occam's Razor, penalizing models with a larger parameter space compared to less flexible models. The key idea of Occam's Razor is that a balance between goodness of fit and model flexibility is desirable, but we emphasise that no special manipulations are required to enforce this balance in the Bayesian approach.

When constructing the parameter space Θ_i, the prior distributions of individual parameters are treated as independent of one another. Although physical relationships among some of these parameters have been described in the literature, the formulation of a coupled prior remains challenging, as these relationships are often convoluted by other properties. For instance, the porosity is generally inversely related to the mean (or median) grain size, but this relationship is convoluted by, e.g., the particle size uniformity (e.g., Wang et al., 2017; Atapour and Mortazavi, 2018; Gupta and Ramanathan, 2018; Díaz-Curiel et al., 2024). As the Bayesian model selection framework already downweights extreme parameter combinations (e.g., high porosity and large grain size) through the chosen independent prior distributions, and because the minimum misfit and most probable parameters are generally consistent with, e.g., the porosity-grain size relationship described in the literature (e.g., Díaz-Curiel et al., 2024), we do not expect a significant change in the posterior probabilities.

Various literature estimates inform the examined parameter ranges and corresponding prior distributions. The porosity prior (Fig. 3a) is derived from borehole data and seismic experiments from Ice Stream B and C, West Antarctica (Blankenship et al., 1987; Engelhardt et al., 1990; Atre and Bentley, 1993), borehole data from Trapridge Glacier, Yukon Territory, Canada (Stone and Clarke, 1993), marine sediment cores from the Amundsen Sea Embayment (Table S1; Smith et al., 2011, 2014, 2017), sediment recovered from beneath Rutford Ice Stream, West Antarctica (Table S1; Smith, unpublished data), as well as the porosity of sands and glass beads used to validate the VGS theory (Buckingham, 2014; Lee et al., 2016, and references therein).
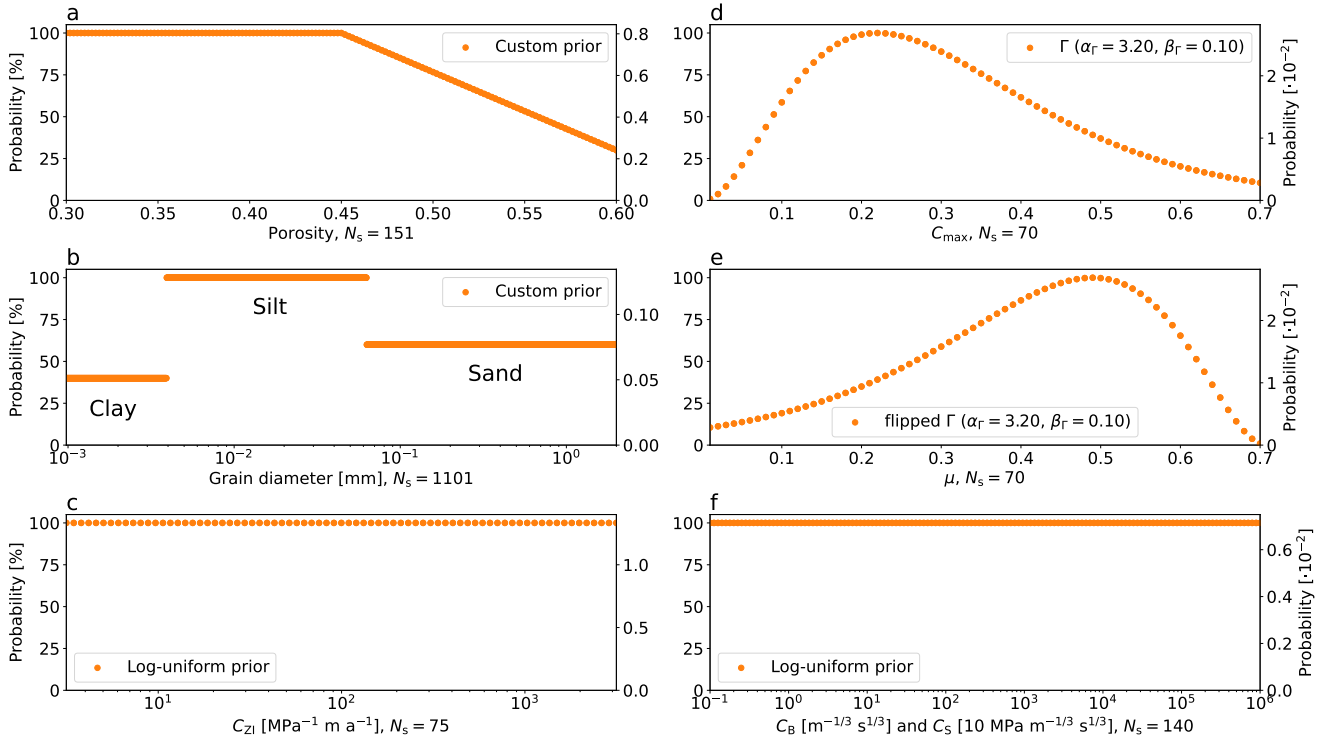
Figure 3. Prior distributions for all model parameters Θ. N_s is the sampling size. The left and right axes show the scaled probability (0 to 100 %) and actual probability used (depends on N_s), respectively.

As the latter do not directly relate to a glacial context, we assign these higher porosities a lower probability. The porosity
255   estimates from seismic experiments (Blankenship et al., 1987; Atre and Bentley, 1993) assume no significant dependence on effective pressure and are employed as an independent comparison rather than to directly inform the prior.

    The grain diameter prior (Fig. 3b) is based on sediment cores collected in the Amundsen Sea Embayment, particularly Pine Island Bay (Table S1; Kirshner et al., 2012; Smith et al., 2011, 2014, 2017; Clark et al., 2024) and the Rutford ice stream (Table S1; Smith, unpublished data). We differentiate between Clay ($< 1/256$ mm), Silt ($\geq 1/256$ mm and $\leq 1/16$ mm), and
260   Sand ($> 1/16$ mm). The prior is then derived from the relative fractions of these grain-size classes.

    The transition speed coefficient (C_{ZI}) values reported in the initial publication of the Zoet-Iverson sliding law range from 56.36 to $363.52\,\mathrm{MPa}^{-1}\,\mathrm{m}\,\mathrm{yr}^{-1}$ (Zoet and Iverson, 2020). A later study using the same bed material (Horicon till sourced from the same location) but with plowing clasts removed uses the same parameters (given in Table S1 of Zoet and Iverson, 2020) except for a smaller clast radius $R = 0.0045$ m (instead of $R = [0.015, 0.030]$ m), leading to $C_{\mathrm{ZI}} = 1120.17\,\mathrm{MPa}^{-1}\,\mathrm{m}\,\mathrm{yr}^{-1}$
265   (Fig. S4 in Hansen et al., 2024). Given these significant uncertainties and that C_{ZI} depends on several other uncertain parameters, a log-uniform prior covering the range 3.16 to $3155.76\,\mathrm{MPa}^{-1}\,\mathrm{m}\,\mathrm{yr}^{-1}$ was chosen (Fig. 3c).

The Due to the range of spatial scales in bed roughness that can affect basal drag, estimating $C_{\max}$ from observations of bed topography is not straightforward. We therefore base our $C_{\max}$ prior (Fig. 3d) is based on 3d) on a combination of coarse-resolution bed topography beneath PIG retrieved from Bedmap2 data (Fig. S7 and S8; Fretwell et al., 2013) (Fig. S7 and S8; Fretwe

270   , as well as high-resolution autonomous underwater vehicle (AUV) data collected downstream of Thwaites Glacier (Graham et al., 2022) (1.5 m; Graham et al., 2022) and under the Thwaites Eastern Ice Shelf (2 m; Wåhlin, unpublished data; Fig. S9 and S10. While S9 and S10). Although shear resistance is most likely built at spatial scales smaller than the resolution of Bedmap2, the bed roughness and therefore the actual relevant scale are less clear and likely vary spatially. As these smaller scales are not explicitly represented by the basal drag derived from our inversion, it is not straightforward to determine the these data provide

275   a conservative lower bound on $C_{\max}$ prior directly from the small-scale AUV data . Therefore, we align the highest probability in the $C_{\max}$ prior with the steepest Bedmap2 bed angles and incorporate even steeper bed angles at smaller scales through a more gradual decline towards higher $C_{\max}$ values (Sec. S6.2).

   μ is a frequently used parameter and its prior (Fig. 3e) aims to capture the overall distribution within the glaciological community (e.g., Savage et al., 2000; Tulaczyk et al., 2000; Cuffey and Paterson., 2010; Iverson, 2010; Tsai et al., 2015;

280   Brondex et al., 2017). Note that although $C_{\max}$ and μ serve similar roles in, e.g., the Schoof and Zoet-Iverson sliding law, they represent distinct physical properties and are thus assigned separate prior distributions (Sec. 2.2.7).

   As C_B and C_S are positive scaling coefficients that may vary over several orders of magnitude, even within the same glacial catchment (Budd et al., 1984; Larour et al., 2012; Favier et al., 2014; Arthern et al., 2015; Brondex et al., 2017; Gladstone et al., 2017), a log-uniform prior was chosen for these parameters (Fig. 3f).

285   Due to the computational cost of the grid search, we currently limit the model parameter space Θ_i to 4D. For example, we do not consider variations in the exponents m, q, and p (Sec. 2.2). However, computationally more efficient methods, such as Monte Carlo algorithms, can be explored in future studies to simultaneously vary more than four parameters.

3   Results and Discussion

3.1   Minimum acoustic impedance misfit comparable for all sliding laws examined

290   Based on a previous study examining the same acoustic impedance data (Kyrke-Smith et al., 2017) and due to the smoothing effect of the inversion (1 km horizontal grid resolution), we do not expect to capture acoustic impedance variations for each individual data point but rather the general trend across the five data sites. Given this context, all sliding laws reasonably match the acoustic impedance observations when using the parameter values yielding the minimum misfit across all data sites (Fig. 4). However, for some sliding laws, the minimum misfit parameter values are at the limits of the likely range (e.g.,

295   extremely small grain diameter ($d_g = 0.003$ mm) for the Budd sliding law). While the minimum misfit might correspond to a rather unlikely parameter value, a narrow band of similarly small misfits spans a more reasonable parameter range, indicating some indistinctness in the selected minimum misfit parameter values. This is a key characteristic of the misfit distribution in all of our experiments. As an example, Fig. 5 shows how the misfit varies with the three model parameters d_g, ϕ, and μ when

using a Coulomb sliding law. The same plots for all other sliding laws with a maximum 3D parameter space are shown in Fig. S11 to S22.
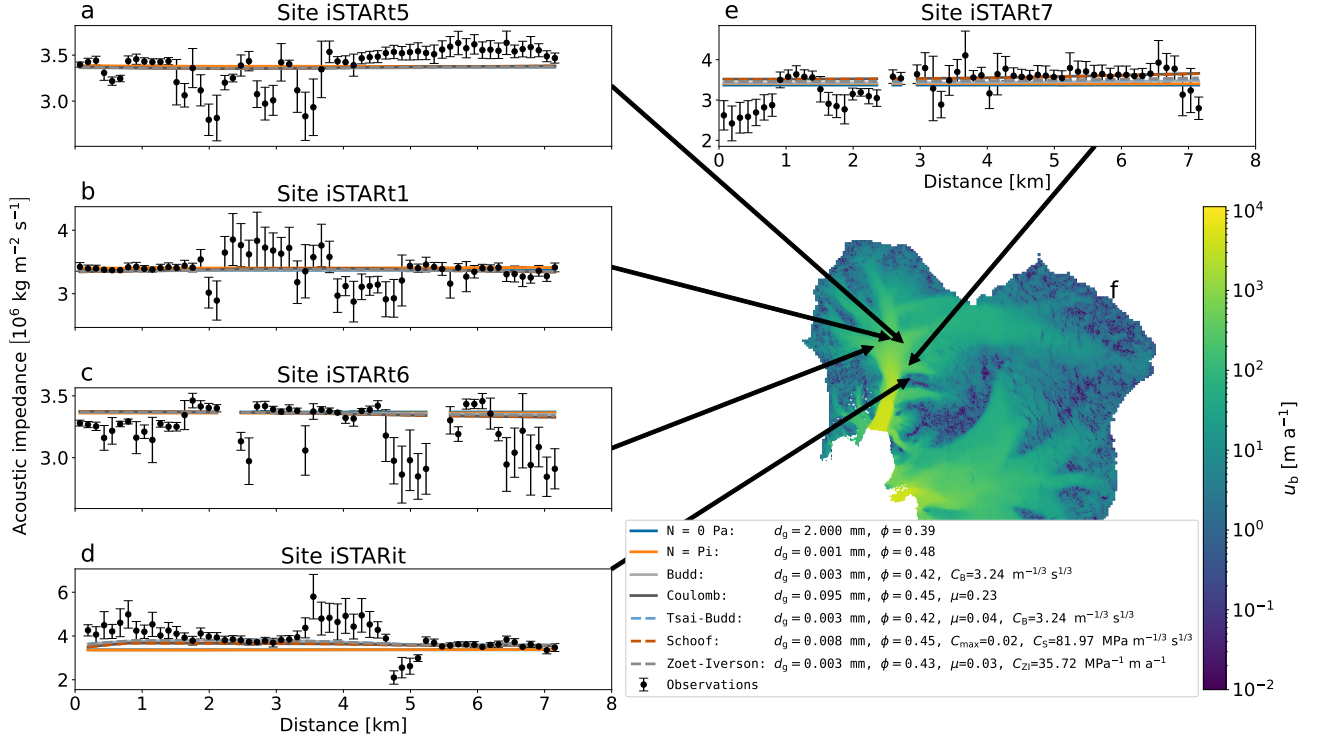
Figure 4. (a-e) Acoustic impedance observations (Brisbourne et al., 2017) compared with the model predictions based on different sliding laws when using the minimum misfit model parameters shown in the legend. The observational uncertainties are shown as error bars. The model parameters are grain diameter (d_g), porosity (ϕ), Budd friction parameter (C_B), Coulomb friction coefficient (μ), Iken's bound (C_{max}), and transition speed coefficient (C_{ZI}; see Sec. 2.2 for details). (f) Basal sliding speed in the Amundsen Sea Embayment (from inversion; Sec. 2.3). The arrows mark the location of the data sites. Except for site iSTARit, all data were collected on fast-flowing tributaries of PIG (Brisbourne et al., 2017).

3.2 Ice dynamics of Pine Island Glacier governed by Coulomb-type sliding

To consider the misfit distribution across the entire parameter range and any prior assessment of the probability of the parameter values used, we infer the best-candidate sliding law based on Bayesian model selection. The Coulomb sliding law has the highest posterior probability of all sliding laws tested (increase of $27.5\,\%$ relative to the prior; Fig. 6). However, the Schoof and Zoet-Iverson sliding laws show a similarly strong increase, hindering the determination of a single-best sliding law. The Tsai-Budd sliding law exhibits the smallest increase ($4.8\,\%$) out of all the laws incorporating a Coulomb friction term of the form μN or $C_{max}N$. Nonetheless, the increase in posterior probability for all sliding laws incorporating a Coulomb friction term suggests this is a desirable property of a sliding law. In comparison, the Budd sliding law, without the μN modification
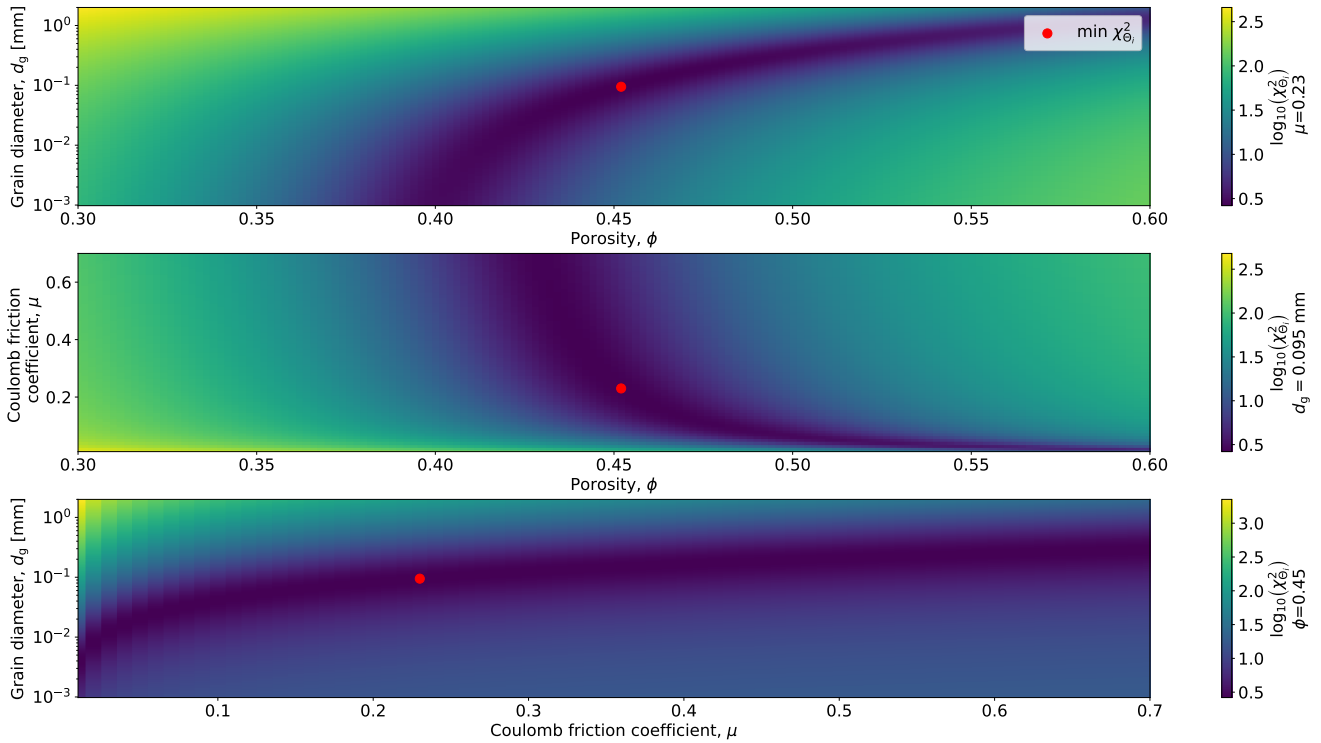
Figure 5. Variations of the misfit $\chi^2_{\Theta_i}$ with the three model parameters grain diameter (d_g), porosity (ϕ), and Coulomb friction coefficient (μ) under a Coulomb sliding law. For the parameter not shown, the value yielding the minimum misfit is used and denoted next to the colorbar of the corresponding panel. The red dots mark the minimum misfit.

of the Tsai-Budd law, performs worse (0.8 % decrease). The fixed effective pressure endmember scenario that assumes $N = p_i$
everywhere performs worst of all, leading to the smallest posterior probability (83.4 % decrease). The endmember scenario
with $N = 0$ Pa everywhere yields the highest posterior probability of all fixed effective pressure experiments (4.1 % increase;
see also Fig. S23).

The relatively high posterior probabilities of sliding laws incorporating a Coulomb friction term and the $N = 0$ Pa end-
member scenario are consistent with the widespread occurrence of deformable sediment under the fast-flowing tributaries of
PIG (Brisbourne et al., 2017). Furthermore, the high probabilities of these sliding laws align with previous studies identifying
(quasi-)plastic deformation of the underlying sediment as the primary mode of sliding for PIG (Gillet-Chaulet et al., 2016;
Joughin et al., 2019). While the sensitivity of grounding-line retreat patterns and mass loss projections to the choice of sliding
law is high (Brondex et al., 2019), determining the exact implications of using a (quasi-)plastic sliding law on glacier behaviour
through prognostic simulations for all sliding laws and parameter values is out of the scope of this study. In general, sliding
laws representing a (quasi-)plastic rheology lead to higher sea level rise contributions (Ritz et al., 2015; Gillet-Chaulet et al.,
2016; Brondex et al., 2019).

Figure 6. Normalized probabilities (Eq. 20) of all sliding laws examined in this study given the acoustic impedance observations collected on PIG. The prior model probability is $P(M_i|I) = 1/n$, with n being the number of models examined (blue circles; dashed horizontal line visualizes equal prior probability). To obtain the posterior model probability, we marginalized over all corresponding model parameters Θ_i, encompassing the acoustic propagation model parameters (d_g and ϕ) and any additional sliding-law-specific parameters (denoted in brackets). No sliding law parameter was varied for the two fixed effective pressure endmember scenarios $N = p_i$ and $N = 0$ Pa. The prior distributions for all parameters are shown in Fig. 3. The blue vertical lines and numbers indicate the change in probability.

3.3 Effect of prior distributions on most probable model parameters and sliding laws

As for the minimum misfit model parameters, the predicted acoustic impedance under the model parameters with the highest posterior probability generally agrees with the observations within uncertainties for all sliding laws tested (Fig. S24). In the
325 remainder of this paper, we refer to the model parameters with the highest posterior probability as the maximum a posteriori (MAP) parameters. When examining the MAP parameters in more detail (Fig. S24), the effect of the chosen prior distributions is evident. Although covering the full range within this size classification, the MAP grain diameter for all sliding laws is Silt-sized (highest prior probability; Fig. 3). The MAP porosities (0.39 to 0.44) are at the upper end of the high-prior probability range ($\phi = [0.3, 0.45]$) for all sliding laws except the fixed effective pressure endmember scenario $N = p_i$ ($\phi = 0.55$; Fig. S24),
330 indicating comparatively porous sediments beneath PIG. Similarly, the MAP values of the unique sliding law parameters without a log-uniform prior distribution (μ and $C_{\max}$) are in the vicinity of the highest prior probability.

Even ~~if we use~~ when using log-uniform prior distributions for scaling coefficients and uniform priors for other parameters ~~,~~ ~~the~~ – thus making no use of the Bedmap2 or AUV data to constrain the $C_{\max}$ prior – the sliding laws incorporating a Coulomb friction term still yield the highest probabilities~~(~~, with the Coulomb and Schoof sliding law showing the greatest increase (26.3 % for both; Fig. S25). This demonstrates the robustness of our key result against variations in prior distributions.

3.4 Low effective pressure across most of Amundsen Sea Embayment

Excluding the fixed effective pressure scenarios, the predicted effective pressure for the MAP model parameters is generally below $0.1\,\mathrm{MPa}\,(1\,\mathrm{bar})$ for the 4 sites within fast-flowing tributaries (Fig. S26). The relatively high probability of the $N = 0\,\mathrm{Pa}$ endmember scenario (Fig. 6 and S23) further supports a low effective pressure. This is in agreement with previous effective pressure estimates derived from, e.g., shear wave velocities (Blankenship et al., 1987), borehole water level measurements (Engelhardt et al., 1990; Engelhardt and Kamb, 1997; Lüthi et al., 2002; Smith et al., 2021), and the widespread presence of active subglacial lakes (Gray et al., 2005; Fricker et al., 2007; Smith et al., 2009).

Site iSTARit, located between two tributaries, has higher effective pressures (0.1 to $1\,\mathrm{MPa}$), with the effective pressure derived from the Coulomb sliding law being $\sim 0.1\,\mathrm{MPa}$. We hypothesize that the higher effective pressure and resulting increased basal drag at this site hinder basal sliding.

Retrieving the effective pressure for the Coulomb sliding law with the MAP parameters across the whole Amundsen Sea Embayment indicates the effective pressure is generally below $0.5\,\mathrm{MPa}$ (Fig. 7b). Being closely related to the basal drag, this map represents the slipperiness of the bed, with areas of low effective pressure being susceptible to fast retreat. However, the effective pressure map is based on a spatially uniform μ obtained from five sites in PIG and does not capture (local) dynamic subglacial systems as, e.g., represented by a subglacial hydrology model. Furthermore, using only the Coulomb sliding law with the MAP parameters neglects the probabilities of other sliding laws and parameter values. Therefore, the provided effective pressure map should be used with caution. Following the Bayesian framework to determine the most probable effective pressure map by weighting the individual maps for all sliding laws and parameter values, incorporating spatially variable model parameters, as well as applying BASLI–VGS in regions characterized by higher basal heterogeneity (e.g., Thwaites Glacier), should be explored in future studies.

4 Conclusions

In this study, we present the new BASLI–VGS approach that directly relates measured and predicted acoustic impedance data. Since the predicted acoustic impedance depends on the effective pressure, an ice sheet sliding law and its parameters can be inferred, subsequently enabling the derivation of an effective pressure map. While the current conclusions are primarily based on seismic data over soft sediments, the presented methodology can be readily applied to any acoustic impedance data collected in glacial environments underlain by granular material. For the seismic data collected on fast-flowing tributaries of Pine Island Glacier, the acoustic propagation model predicts the observed acoustic impedance within uncertainties. Inferred effective pressures are generally below $0.5\,\mathrm{MPa}$ across most of the Amundsen Sea Embayment and below $0.1\,\mathrm{MPa}$ within fast-
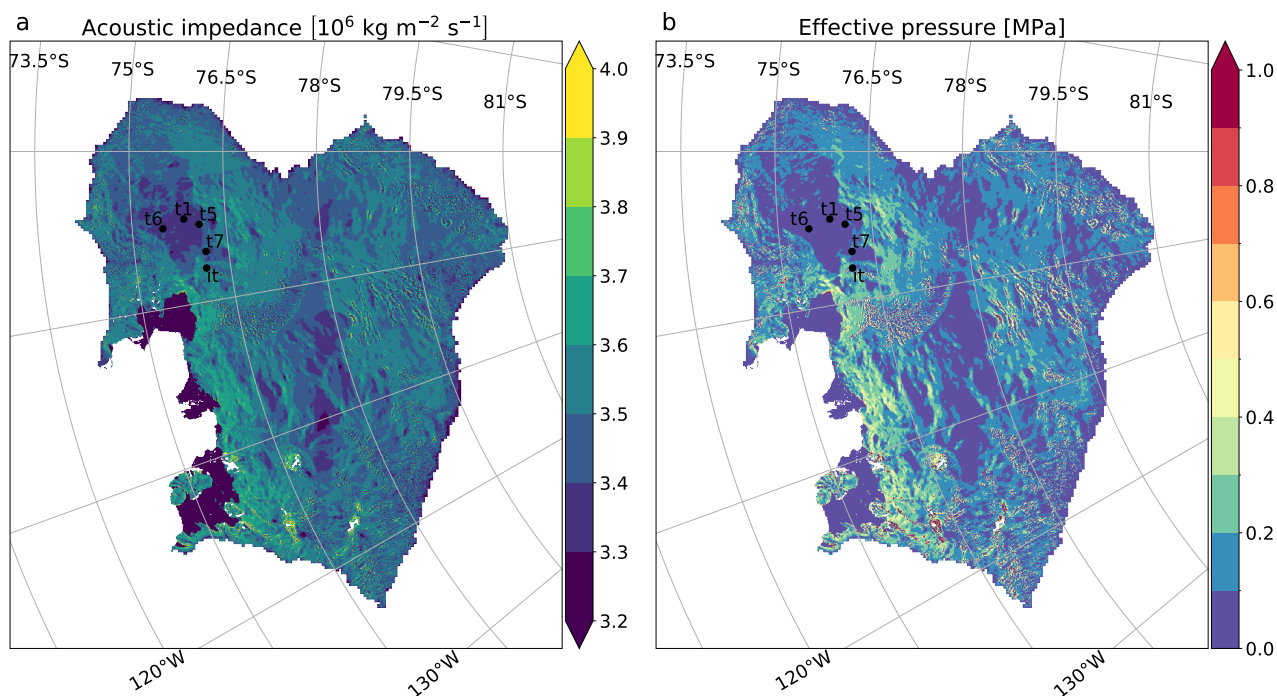
Figure 7. Predicted acoustic impedance (a) and effective pressure (b) in the Amundsen Sea Embayment when using a Coulomb sliding law with the MAP (highest posterior probability) model parameters ($d_\mathrm{g} = 0.063$ mm, $\phi = 0.43$, and $\mu = 0.49$). The black dots mark the locations of the seismic observation sites.

flowing tributaries of Pine Island Glacier. Bayesian model selection identifies Coulomb behaviour as the most probable mode

365 of sliding, potentially increasing sea level rise contributions from the Amundsen Sea Embayment. To minimize uncertainties in sea level rise projections, the sliding law used in large-scale ice sheet models should, therefore, approach Coulomb behaviour in fast-flowing regions.

Code availability. The code is available at https://doi.org/10.5281/zenodo.17549775.

Data availability. The data is available at https://doi.org/10.5285/c560ce43-7aa0-4474-90ed-d4ee5f5768ea.

370 *Code and data availability.* TEXT

Sample availability. TEXT

Video supplement. TEXT

Author contributions. KH, RJA, and CRW conceptualized the ideas behind this study. AMB, JAS, and AW prepared, respectively, the seismic data, sediment core data, and AUV data for use in this study. KH prepared the experimental design, ran the model, and analyzed the results
375 with input from all authors. All authors contributed to the interpretation of the results and writing of the paper.

Competing interests. The authors have no competing interests.

Disclaimer. TEXT

Acknowledgements. The authors thank the members of the International Thwaites Glacier Collaboration (ITGC), particularly the ITGC Geophysical Habitat of Subglacial Thwaites (GHOST) team for fruitful discussion. We also thank Ronan S. Agnew and Kelly A. Hogan for
380 their support in the interpretation of acoustic impedance and autonomous underwater vehicle (AUV) data, respectively. Finally, we thank two anonymous reviewers and the handling topic editor, Adam Booth, for their constructive comments.

This work was funded by the GHOST project, a component of the International Thwaites Glacier Collaboration (ITGC). Support from National Science Foundation (NSF: Grant PLR 1738934) and Natural Environment Research Council (NERC: Grant NE/S006672/1), with logistics provided by NSF-U.S. Antarctic Program and NERC-British Antarctic Survey. ITGC Contribution No. ITGC-142. Additional
385 support was provided by the ITGC MELT project (NSF Grant 1739003 and NERC Grant NE/S006656/1) and Natural Environment Research Council (NERC: Grant NE/G014159/1 and NE/R016038/1). The Ran AUV was financed by Knut and Alice Wallenberg Foundation.

References

Arthern, R. J. and Williams, C. R.: The sensitivity of West Antarctica to the submarine melting feedback, Geophysical Research Letters, 44, 2352–2359, https://doi.org/10.1002/2017GL072514, 2017.

390   Arthern, R. J., P. Winebrenner, D., and Vaughan, D.: Antarctic Snow Accumulation Mapped Using Polarization of 4.3-cm Wavelength Microwave Emission, Journal of Geophysical Research, 111, D06 108, https://doi.org/10.1029/2004JD005667, 2006.

Arthern, R. J., Hindmarsh, R. C., and Williams, C. R.: Flow speed within the Antarctic ice sheet and its controls inferred from satellite observations, Journal of Geophysical Research: Earth Surface, 120, 1171–1188, https://doi.org/10.1002/2014JF003239, 2015.

Atapour, H. and Mortazavi, A.: The effect of grain size and cement content on index properties of weakly solidified artificial sandstones, 395   Journal of Geophysics and Engineering, 15, 613, https://doi.org/10.1088/1742-2140/aaa14a, 2018.

Atre, S. R. and Bentley, C. R.: Laterally varying basal conditions beneath ice Streams B and C, West Antarctica, Journal of Glaciology, 39, 507–514, https://doi.org/10.3189/s0022143000016403, 1993.

Barnes, J. M. and Gudmundsson, G. H.: The predictive power of ice sheet models and the regional sensitivity of ice loss to basal sliding parameterisations: a case study of Pine Island and Thwaites glaciers, West Antarctica, The Cryosphere, 16, 4291–4304, 400   https://doi.org/10.5194/tc-16-4291-2022, 2022.

Blankenship, D. D., Bentley, C. R., Rooney, S. T., and Alley, R. B.: Till beneath ice stream B. 1. Properties derived from seismic travel times, Journal of Geophysical Research, 92, 8903–8911, https://doi.org/10.1029/JB092iB09p08903, 1987.

Bradley, A. T., Arthern, R. J., Bett, D. T., Williams, C. R., and Byrne, J.: WAVI.jl: Ice Sheet Modelling in Julia, Journal of Open Source Software, 9, 5584, https://doi.org/10.21105/joss.05584, 2024.

405   Brisbourne, A. M., Smith, A. M., Vaughan, D. G., King, E. C., Davies, D., Bingham, R. G., Smith, E. C., Nias, I. J., and Rosier, S. H.: Bed conditions of Pine Island Glacier, West Antarctica, Journal of Geophysical Research: Earth Surface, 122, 419–433, https://doi.org/10.1002/2016JF004033, 2017.

Brondex, J., Gagliardini, O., Gillet-Chaulet, F., and Durand, G.: Sensitivity of grounding line dynamics to the choice of the friction law, Journal of Glaciology, 63, 854–866, https://doi.org/10.1017/jog.2017.51, 2017.

410   Brondex, J., Gillet-Chaulet, F., and Gagliardini, O.: Sensitivity of centennial mass loss projections of the Amundsen basin to the friction law, The Cryosphere, 13, 177–195, https://doi.org/10.5194/tc-13-177-2019, 2019.

Buckingham, M. J.: Theory of acoustic attenuation, dispersion, and pulse propagation in unconsolidated granular materials including marine sediments, The Journal of the Acoustical Society of America, 1997.

Buckingham, M. J.: Wave propagation, stress relaxation, and grain-to-grain shearing in saturated, unconsolidated marine sediments, 2000.

415   Buckingham, M. J.: Compressional and shear wave properties of marine sediments: Comparisons between theory and data, The Journal of the Acoustical Society of America, 117, 137–152, https://doi.org/10.1121/1.1810231, 2005.

Buckingham, M. J.: On pore-fluid viscosity and the wave properties of saturated granular materials including marine sediments, The Journal of the Acoustical Society of America, 122, 1486–1501, https://doi.org/10.1121/1.2759167, 2007.

Buckingham, M. J.: Analysis of shear-wave attenuation in unconsolidated sands and glass beads, The Journal of the Acoustical Society of 420   America, 136, 2478–2488, https://doi.org/10.1121/1.4896468, 2014.

Budd, W. F., Keage, P. L., and Blundy, N. A.: Empirical Studies of Ice Sliding, Journal of Glaciology, 23, 157–170, https://doi.org/10.3189/s0022143000029804, 1979.

Budd, W. F., Jenssen, D., and Smith, I. N.: A Three-Dimensional Time-Dependent Model of the West Antarctic Ice Sheet, Annals of Glaciology, 5, 29–36, https://doi.org/10.3189/1984aog5-1-29-36, 1984.

Clark, R. W., Wellner, J. S., Hillenbrand, C. D., Totten, R. L., Smith, J. A., Miller, L. E., Larter, R. D., Hogan, K. A., Graham, A. G., Nitsche, F. O., Lehrmann, A. A., Lepp, A. P., Kirkham, J. D., Fitzgerald, V. T., Garcia-Barrera, G., Ehrmann, W., and Wacker, L.: Synchronous retreat of Thwaites and Pine Island glaciers in response to external forcings in the presatellite era, Proceedings of the National Academy of Sciences of the United States of America, 121, https://doi.org/10.1073/pnas.2211711120, 2024.

Cornford, S. L., Martin, D. F., Graves, D. T., Ranken, D. F., Le Brocq, A. M., Gladstone, R. M., Payne, A. J., Ng, E. G., and Lipscomb, W. H.: Adaptive mesh, finite volume modeling of marine ice sheets, Journal of Computational Physics, 232, 529–549, https://doi.org/https://doi.org/10.1016/j.jcp.2012.08.037, 2013.

Cuffey, K. and Paterson., W.: The Physics of Glaciers, Butterworth-Heinemann/Elsevier, Burlington, MA, 4th edn., 2010.

Díaz-Curiel, J., Biosca, B., Arévalo-Lomas, L., Paredes-Palacios, D., and Miguel, M. J.: On the Influence of Grain Size Compared with Other Internal Factors Affecting the Permeability of Granular Porous Media: Redefining the Permeability Units, Lithosphere, 2024, lithosphere_2023_231, https://doi.org/10.2113/2024/lithosphere_2023_231, 2024.

Engelhardt, H. and Kamb, B.: Basal hydraulic system of a west Antarctic ice stream: constraints from borehole observations, Journal of Glaciology, 43, 207–230, https://doi.org/10.3189/s0022143000003166, 1997.

Engelhardt, H., Humphrey, N., Kamb, B., and Fahnestock, M.: Physical Conditions at the Base of a Fast Moving Antarctic Ice Stream, Science, 248, 57–59, https://doi.org/10.1126/science.248.4951.57, 1990.

Favier, L., Durand, G., Cornford, S. L., Gudmundsson, G. H., Gagliardini, O., Gillet-Chaulet, F., Zwinger, T., Payne, A. J., and Brocq, A. M. L.: Retreat of Pine Island Glacier controlled by marine ice-sheet instability, Nature Climate Change, 4, 117–121, https://doi.org/10.1038/nclimate2094, 2014.

Fowler, A. C.: Instability modelling of drumlin formation incorporating lee-side cavity growth, Proceedings of the Royal Society A: Mathematical, Physical and Engineering Sciences, 465, 2681–2702, https://doi.org/10.1098/rspa.2008.0490, 2009.

Fretwell, P., Pritchard, H. D., Vaughan, D. G., Bamber, J. L., Barrand, N. E., Bell, R., Bianchi, C., Bingham, R. G., Blankenship, D. D., Casassa, G., Catania, G., Callens, D., Conway, H., Cook, A. J., Corr, H. F., Damaske, D., Damm, V., Ferraccioli, F., Forsberg, R., Fujita, S., Gim, Y., Gogineni, P., Griggs, J. A., Hindmarsh, R. C., Holmlund, P., Holt, J. W., Jacobel, R. W., Jenkins, A., Jokat, W., Jordan, T., King, E. C., Kohler, J., Krabill, W., Riger-Kusk, M., Langley, K. A., Leitchenkov, G., Leuschen, C., Luyendyk, B. P., Matsuoka, K., Mouginot, J., Nitsche, F. O., Nogi, Y., Nost, O. A., Popov, S. V., Rignot, E., Rippin, D. M., Rivera, A., Roberts, J., Ross, N., Siegert, M. J., Smith, A. M., Steinhage, D., Studinger, M., Sun, B., Tinto, B. K., Welch, B. C., Wilson, D., Young, D. A., Xiangbin, C., and Zirizzotti, A.: Bedmap2: Improved ice bed, surface and thickness datasets for Antarctica, Cryosphere, 7, 375–393, https://doi.org/10.5194/tc-7-375-2013, 2013.

Fricker, H. A., Scambos, T., Bindschadler, R., and Padman, L.: An Active Subglacial Water System in West Antarctica Mapped from Space, Science, 315, 1544–1548, https://doi.org/10.1126/science.1136897, 2007.

Gagliardini, O., Cohen, D., Råback, P., and Zwinger, T.: Finite-element modeling of subglacial cavities and related friction law, Journal of Geophysical Research: Earth Surface, 112, https://doi.org/10.1029/2006JF000576, 2007.

Gillet-Chaulet, F., Durand, G., Gagliardini, O., Mosbeux, C., Mouginot, J., Rémy, F., and Ritz, C.: Assimilation of surface velocities acquired between 1996 and 2010 to constrain the form of the basal friction law under Pine Island Glacier, Geophysical Research Letters, 43, 10,311–10,321, https://doi.org/10.1002/2016GL069937, 2016.

Gladstone, R. M., Warner, R. C., Galton-Fenzi, B. K., Gagliardini, O., Zwinger, T., and Greve, R.: Marine ice sheet model performance depends on basal sliding physics and sub-shelf melting, Cryosphere, 11, 319–329, https://doi.org/10.5194/tc-11-319-2017, 2017.

Graham, A. G., Wåhlin, A., Hogan, K. A., Nitsche, F. O., Heywood, K. J., Totten, R. L., Smith, J. A., Hillenbrand, C. D., Simkins, L. M., Anderson, J. B., Wellner, J. S., and Larter, R. D.: Rapid retreat of Thwaites Glacier in the pre-satellite era, Nature Geoscience, 15, 706–713, https://doi.org/10.1038/s41561-022-01019-9, 2022.

Granick, S.: Soft matter in a tight spot, Physics Today, 52, 26–31, https://doi.org/10.1063/1.882747, 1999.

465 Gray, L., Joughin, I., Tulaczyk, S., Spikes, V. B., Bindschadler, R., and Jezek, K.: Evidence for subglacial water transport in the West Antarctic Ice Sheet through three-dimensional satellite radar interferometry, Geophysical Research Letters, 32, 1–4, https://doi.org/10.1029/2004GL021387, 2005.

Gudmundsson, G. H., Paolo, F. S., Adusumilli, S., and Fricker, H. A.: Instantaneous Antarctic ice sheet mass loss driven by thinning ice shelves, Geophysical Research Letters, 46, 13 903–13 909, https://doi.org/https://doi.org/10.1029/2019GL085027, 2019.

470 Gupta, A. and Ramanathan, A. L.: Grain texture as a proxy to understand porosity, permeability and density in Chandra Basin, India, SN Applied Sciences, 1, 1, https://doi.org/10.1007/s42452-018-0001-3, 2018.

Hank, K. and Tarasov, L.: The comparative role of physical system processes in Hudson Strait ice stream cycling: a comprehensive model-based test of Heinrich event hypotheses, Climate of the Past, 20, 2499–2524, https://doi.org/10.5194/cp-20-2499-2024, 2024.

Hansen, D. D., Warburton, K. L. P., Zoet, L. K., Meyer, C. R., Rempel, A. W., and Stubblefield, A. G.: Presence of Frozen Fringe Impacts Soft-
475 Bedded Slip Relationship, Geophysical Research Letters, 51, e2023GL107 681, https://doi.org/https://doi.org/10.1029/2023GL107681, e2023GL107681 2023GL107681, 2024.

Hoffman, M. J., Perego, M., Price, S. F., Lipscomb, W. H., Zhang, T., Jacobsen, D., Tezaur, I., Salinger, A. G., Tuminaro, R., and Bertagna, L.: MPAS-Albany Land Ice (MALI): a variable-resolution ice sheet model for Earth system modeling using Voronoi grids, Geoscientific Model Development, 11, 3747–3780, https://doi.org/10.5194/gmd-11-3747-2018, 2018.

480 Iken, A.: The Effect of the Subglacial Water Pressure on the Sliding Velocity of a Glacier in an Idealized Numerical Model, Journal of Glaciology, 27, 407–421, https://doi.org/10.3189/s0022143000011448, 1981.

IPCC Core Writing Team, H. Lee and J. Romero (eds.): IPCC 2023: Summary for Policymakers. In: Climate Change 2023: Synthesis Report. Contribution of Working Groups I, II and III to the Sixth Assessment Report of the Intergovernmental Panel on Climate Change, IPCC, Geneva, Switzerland, https://doi.org/10.59327/IPCC/AR6-9789291691647.001, 2023.

485 Israelachvili, J. N.: Measurements of the viscosity of thin fluid films between two surfaces with and without adsorbed polymers, 1986.

Iverson, N. R.: Shear resistance and continuity of subglacial till: Hydrology rules, https://doi.org/10.3189/002214311796406220, 2010.

Iverson, N. R., Hoover, T. S., and Baker, R. W.: Ring-shear studies of till deformation: Coulomb-plastic behavior and distributed strain in glacier beds, Journal of Glaciology, 44, 634–642, https://doi.org/10.1017/S0022143000002136, 1998.

Joughin, I., Smith, B. E., and Schoof, C. G.: Regularized Coulomb Friction Laws for Ice Sheet Sliding: Application to Pine Island Glacier,
490 Antarctica, Geophysical Research Letters, 46, 4764–4771, https://doi.org/10.1029/2019GL082526, 2019.

Kirshner, A. E., Anderson, J. B., Jakobsson, M., O'Regan, M., Majewski, W., and Nitsche, F. O.: Post-LGM deglaciation in Pine Island Bay, West Antarctica, Quaternary Science Reviews, 38, 11–26, https://doi.org/10.1016/j.quascirev.2012.01.017, 2012.

Kyrke-Smith, T. M., Gudmundsson, G. H., and Farrell, P. E.: Can Seismic Observations of Bed Conditions on Ice Streams Help Constrain Parameters in Ice Flow Models?, Journal of Geophysical Research: Earth Surface, 122, 2269–2282, https://doi.org/10.1002/2017JF004373,
495 2017.

Larour, E., Schiermeier, J., Rignot, E., Seroussi, H., Morlighem, M., and Paden, J.: Sensitivity Analysis of Pine Island Glacier ice flow using ISSM and DAKOTA, Journal of Geophysical Research: Earth Surface, 117, https://doi.org/10.1029/2011JF002146, 2012.

Lee, K. M., Ballard, M. S., McNeese, A. R., Muir, T. G., Wilson, P. S., Costley, R. D., and Hathaway, K. K.: In situ measurements of sediment acoustic properties in Currituck Sound and comparison to models, The Journal of the Acoustical Society of America, 140, 3593–3606, https://doi.org/10.1121/1.4966118, 2016.

Lliboutry, L.: Contribution à la théorie du frottement du glacier sur son lit, CR Hebd. Séances Acad. Sci, 247, 318–320, 1958a.

Lliboutry, L.: Frottement sur le lit et mouvement par saccades d'un glacier, CR Hebd. Seances Acad. Sci, 247, 228–230, 1958b.

Lliboutry, L.: Une théorie du frottement du glacier sur son lit, in: Annales de Géophysique, vol. 15, p. 250, 1959.

Luengo, G., Lsraelachvili, J., and Granick, S.: Generalized effects in confined fluids: new friction map for boundary lubrication, 1996.

Lüthi, M., Funk, M., Iken, A., Gogineni, S., and Truffer, M.: Mechanisms of fast flow in Jakobshavn Isbræ, West Greenland: Part III. Measurements of ice deformation, temperature and cross-borehole conductivity in boreholes to the bedrock, Journal of Glaciology, 48, 369–385, https://doi.org/10.3189/172756502781831322, 2002.

Mouginot, J., Scheuchl, B., and Rignot., E.: MEaSUREs Annual Antarctic Ice Velocity Maps 2005-2017, Version 1. 2014/5]., https://doi.org/10.5067/9T4EPQXTJYW9, 2022.

Muto, A., Peters, L. E., Gohl, K., Sasgen, I., Alley, R. B., Anandakrishnan, S., and Riverman, K. L.: Subglacial bathymetry and sediment distribution beneath Pine Island Glacier ice shelf modeled using aerogravity and in situ geophysical data: New results, Earth and Planetary Science Letters, 433, 63–75, https://doi.org/https://doi.org/10.1016/j.epsl.2015.10.037, 2016.

Nias, I. J., Cornford, S. L., and Payne, A. J.: New Mass-Conserving Bedrock Topography for Pine Island Glacier Impacts Simulated Decadal Rates of Mass Loss, Geophysical Research Letters, 45, 3173–3181, https://doi.org/https://doi.org/10.1002/2017GL076493, 2018.

Ranganathan, M., Minchew, B., Meyer, C. R., and Gudmundsson, G. H.: A new approach to inferring basal drag and ice rheology in ice streams, with applications to West Antarctic Ice Streams, Journal of Glaciology, 67, 229–242, https://doi.org/10.1017/jog.2020.95, 2021.

Richardson, M. D., Briggs, K. B., Bibee, L. D., Jumars, P. A., Sawyer, W. B., Albert, D. B., Bennett, R. H., Berger, T. K., Buckingham, M. J., Chotiros, N. P., Dahl, P. H., Dewitt, N. T., Fleischer, P., Flood, R., Greenlaw, C. F., Holliday, D. V., Hulbert, M. H., Hutnak, M. P., Jackson, P. D., Jaffe, J. S., Johnson, H. P., Lavoie, D. L., Lyons, A. P., Martens, C. S., Mcgehee, D. E., Moore, K. D., Orsi, T. H., Piper, J. N., Ray, R. I., Reed, A. H., Self, R. F. L., Schmidt, J. L., Schock, S. G., Simonet, F., Stoll, R. D., Tang, D., Thistle, D. E., Thorsos, E. I., Walter, D. J., Wheatcroft, R. A., Richardson, M. D., Briggs, K. B., Bibee, L. D., Sawyer, W. B., Lavoie, D. L., Ray, R. I., Reed, A. H., Walter, D. J., Jumars, P. A., Albert, D. B., Martens, C. S., Buckingham, M. J., Dahl, P. H., Tang, D., and Thorsos, E. I.: Overview of SAX99: Environmental Considerations, 2001.

Ritz, C., Edwards, T. L., Durand, G., Payne, A. J., Peyaud, V., and Hindmarsh, R. C.: Potential sea-level rise from Antarctic ice-sheet instability constrained by observations, Nature, 528, 115–118, https://doi.org/10.1038/nature16147, 2015.

Savage, W., Morrissey, M., and andRL Baum: Geotechnical Properties for Landslide-Prone Seattle Area Glacial Deposits, U.S. Geological Survey, 2000.

Schoof, C.: The effect of cavitation on glacier sliding, Proceedings of the Royal Society A: Mathematical, Physical and Engineering Sciences, 461, 609–627, https://doi.org/10.1098/rspa.2004.1350, 2005.

Schoof, C.: Cavitation on Deformable Glacier Beds, SIAM Journal on Applied Mathematics, 67, 1633–1653, https://doi.org/10.1137/050646470, 2007a.

Schoof, C.: Pressure-dependent viscosity and interfacial instability in coupled ice–sediment flow, Journal of Fluid Mechanics, 570, 227–252, https://doi.org/10.1017/S0022112006002874, 2007b.

Schoof, C., Hewitt, I. J., and Werder, M. A.: Flotation and free surface flow in a model for subglacial drainage. Part 1. Distributed drainage, Journal of Fluid Mechanics, 702, 126–156, https://doi.org/10.1017/jfm.2012.165, 2012.

Smith, A. M., Jordan, T. A., Ferraccioli, F., and Bingham, R. G.: Influence of subglacial conditions on ice stream dynamics: Seismic and potential field data from Pine Island Glacier, West Antarctica, Journal of Geophysical Research: Solid Earth, 118, 1471–1482, https://doi.org/https://doi.org/10.1029/2012JB009582, 2013.

Smith, A. M., Anker, P. G. D., Nicholls, K. W., Makinson, K., Murray, T., Rios-Costas, S., Brisbourne, A. M., Hodgson, D. A., Schlegel, R., and Anandakrishnan, S.: Ice stream subglacial access for ice-sheet history and fast ice flow: the BEAMISH Project on Rutford Ice Stream, West Antarctica and initial results on basal conditions, Annals of Glaciology, 62, 203–211, https://doi.org/10.1017/aog.2020.82, 2021.

Smith, B., Fricker, H. A., Gardner, A. S., Medley, B., Nilsson, J., Paolo, F. S., Holschuh, N., Adusumilli, S., Brunt, K., Csatho, B., Harbeck, K., Markus, T., Neumann, T., R, S. M., and Zwally, H. J.: Pervasive ice sheet mass loss reflects competing ocean and atmosphere processes, Science, 368, 1239–1242, contains maps of thinning rates in Antarctica, demonstrating the significant thinning of WAIS over the satellite period., 2020.

Smith, B. E., Fricker, H. A., Joughin, I. R., and Tulaczyk, S.: An inventory of active subglacial lakes in Antarctica detected by ICESat (2003-2008, Journal of Glaciology, 55, 573–595, https://doi.org/10.3189/002214309789470879, 2009.

Smith, J. A., Hillenbrand, C.-D., Kuhn, G., Larter, R. D., Graham, A. G., Ehrmann, W., Moreton, S. G., and Forwick, M.: Deglacial history of the West Antarctic Ice Sheet in the western Amundsen Sea Embayment, Quaternary Science Reviews, 30, 488–505, https://doi.org/https://doi.org/10.1016/j.quascirev.2010.11.020, 2011.

Smith, J. A., Hillenbrand, C. D., Kuhn, G., Klages, J. P., Graham, A. G., Larter, R. D., Ehrmann, W., Moreton, S. G., Wiers, S., and Frederichs, T.: New constraints on the timing of West Antarctic Ice Sheet retreat in the eastern Amundsen Sea since the Last Glacial Maximum, Global and Planetary Change, 122, 224–237, https://doi.org/10.1016/j.gloplacha.2014.07.015, 2014.

Smith, J. A., Andersen, T. J., Shortt, M., Gaffney, A. M., Truffer, M., Stanton, T. P., Bindschadler, R., Dutrieux, P., Jenkins, A., Hillenbrand, C. D., Ehrmann, W., Corr, H. F., Farley, N., Crowhurst, S., and Vaughan, D. G.: Sub-ice-shelf sediments record history of twentieth-century retreat of Pine Island Glacier, Nature, 541, 77–80, https://doi.org/10.1038/nature20136, 2017.

Stone, D. B. and Clarke, G. K.: Estimation of subglacial hydraulic properties from induced changes in basal water pressure: a theoretical framework for borehole-response tests, Journal of Glaciology, 39, 327–340, https://doi.org/10.3189/s0022143000015999, 1993.

Tsai, V. C., Stewart, A. L., and Thompson, A. F.: Marine ice-sheet profiles and stability under Coulomb basal conditions, Journal of Glaciology, 61, 205–215, https://doi.org/10.3189/2015JoG14J221, 2015.

Tulaczyk, S., Kamb, W. B., and Engelhardt, H. F.: Basal mechanics of Ice Stream B, West Antarctica 1. Till mechanics, Journal of Geophysical Research: Solid Earth, 105, 463–481, https://doi.org/10.1029/1999jb900329, 2000.

Wang, J.-P., François, B., and Lambert, P.: Equations for hydraulic conductivity estimation from particle size distribution: A dimensional analysis, Water Resources Research, 53, 8127–8134, https://doi.org/https://doi.org/10.1002/2017WR020888, 2017.

Weertman, J.: On the Sliding of Glaciers, Journal of Glaciology, 3, 33–38, https://doi.org/10.3189/s0022143000024709, 1957.

Yamada, S.: Layering transitions and tribology of molecularly thin films of poly(dimethylsiloxane), Langmuir, 19, 7399–7405, https://doi.org/10.1021/la034511l, 2003.

Zoet, L. K. and Iverson, N. R.: A slip law for glaciers on deformable beds, Science, 368, https://doi.org/10.1126/science.aaz1183, 2020.

S1 Basal ice speed and basal drag map
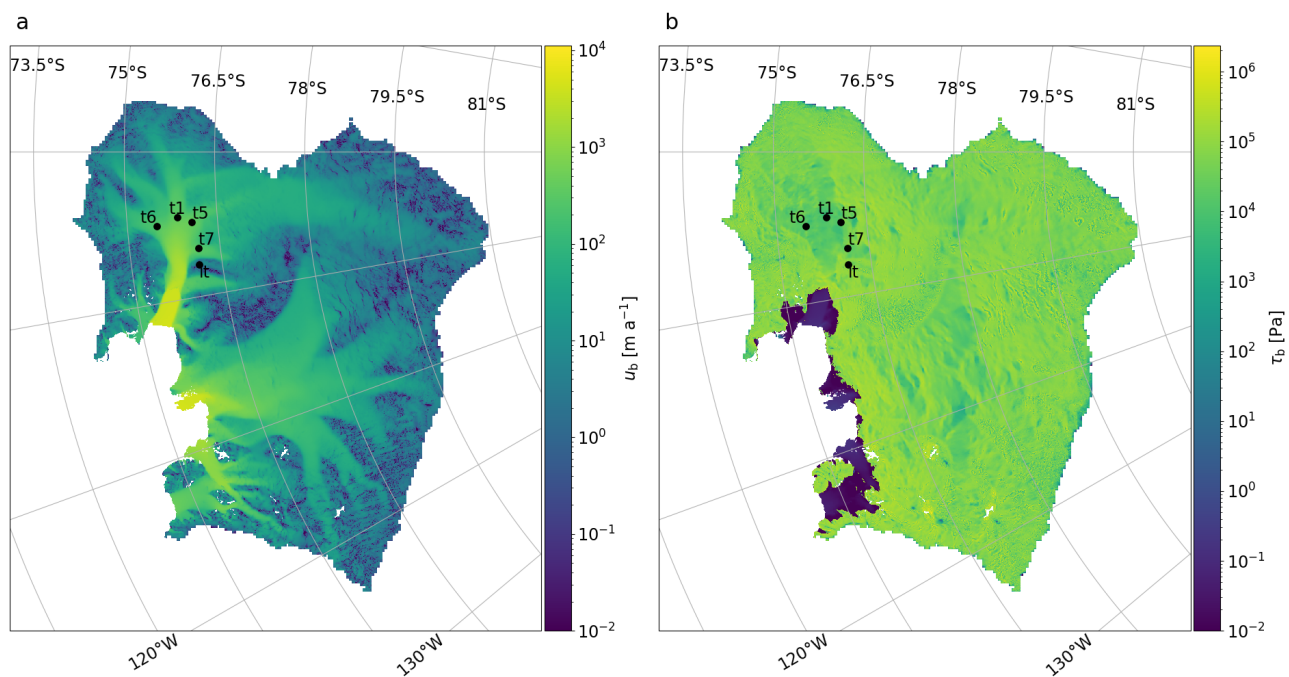
Figure S1. Basal sliding speed (a) and basal shear stress (b) in the Amundsen Sea Embayment retrieved from the surface-to-bed inversion. The black dots mark the locations of the seismic observation sites.

S2 Posterior probabilities when using sub-sampled data
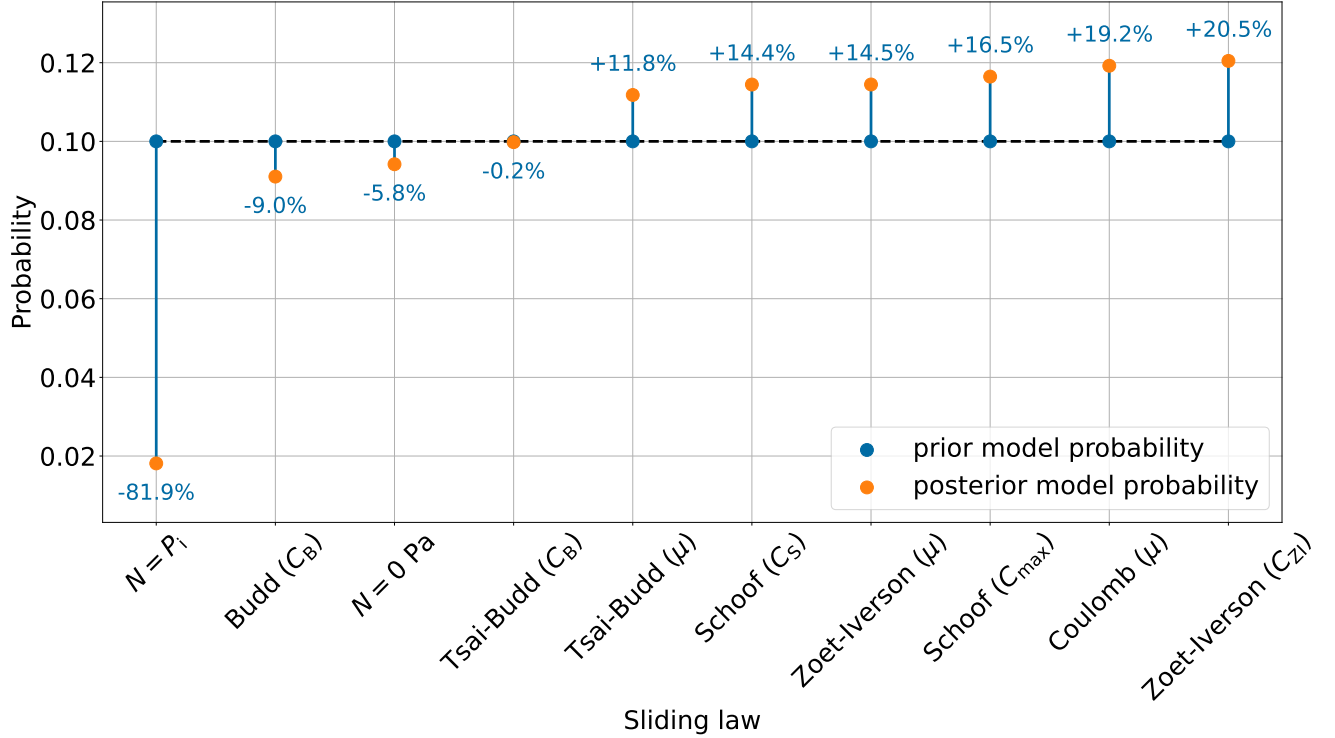
Figure S2. Normalized probabilities (Eq. 20) when using only every 10th acoustic impedance measurement collected on Pine Island Glacier (PIG). Due to the small changes in the posterior model probabilities (Fig. S3) but significant increases in computational cost, we did not run sub-sampled experiments for the 4D sliding laws. Limiting Θ_i to 3D leads to two different representations of the Tsai-Budd, Schoof, and Zoet-Iverson sliding law with one sliding law parameter fixed. The fixed parameters are $\mu = 0.5$ for Tsai-Budd (C_B), $C_B = 37.01$ m$^{-1/3}$ s$^{1/3}$ (based on minimum misfit when varying C_B) for Tsai-Budd (μ), $C_{max} = 0.2$ for Schoof (C_S), $C_S = 1 \cdot 10^3$ MPa m$^{-1/3}$ s$^{1/3}$ (value closest to $C_S = 7.624$ MPa m$^{-1/3}$ s$^{1/3}$ suggested by Brondex et al. (2017) while ensuring low percentage of incompatible $u_b - \tau_b$ pairs; Sec. S5; Fig S15 and S16) for Schoof (C_{max}), $\mu = 0.5$ for Zoet-Iverson (C_{ZI}), and $C_{ZI} \sim 340$ MPa^{-1} m a^{-1} (as suggested by Zoet and Iverson, 2020) for Zoet-Iverson (μ). Unless indicated otherwise, these values correspond to the highest prior probability. Otherwise, as Fig. 6 in the main text.

S3 3D-4D parameter space comparison
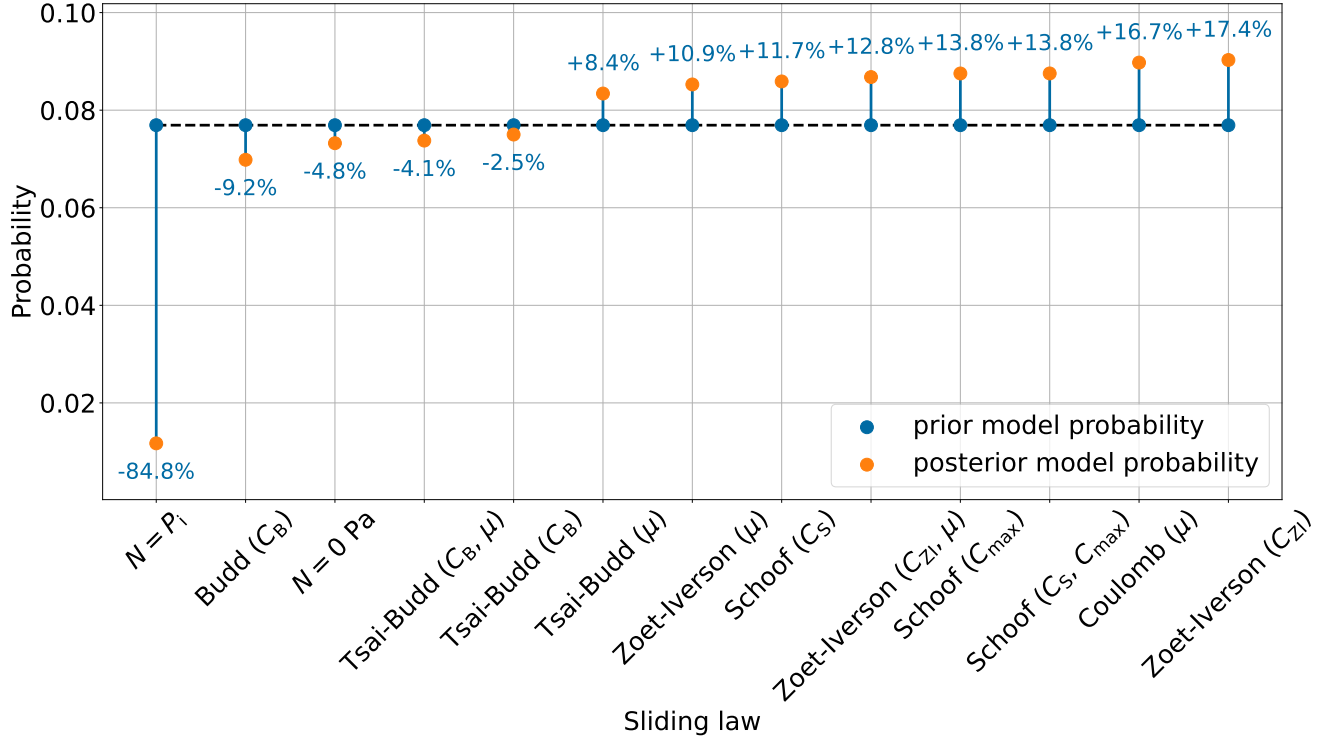
Figure S3. Normalized probabilities (Eq. 20) when limiting the model parameter space Θ_i to 3D compared to the full 4D results. Limiting Θ_i to 3D leads to two different representations of the Tsai-Budd, Schoof, and Zoet-Iverson sliding law with one sliding law parameter fixed. The fixed parameters are $\mu = 0.5$ for Tsai-Budd (C_B), $C_B = 37.01$ m$^{-1/3}$ s$^{1/3}$ (based on minimum misfit when varying C_B) for Tsai-Budd (μ), $C_{max} = 0.2$ for Schoof (C_S), $C_S = 1 \cdot 10^3$ MPa m$^{-1/3}$ s$^{1/3}$ (value closest to $C_S = 7.624$ MPa m$^{-1/3}$ s$^{1/3}$ suggested by Brondex et al. (2017) while ensuring low percentage of incompatible $u_b - \tau_b$ pairs; Sec. S5; Fig S15 and S16) for Schoof (C_{max}), $\mu = 0.5$ for Zoet-Iverson (C_{ZI}), and $C_{ZI} \sim 340$ MPa^{-1} m a^{-1} (as suggested by Zoet and Iverson, 2020) for Zoet-Iverson (μ). Unless indicated otherwise, these values correspond to the highest prior probability. Otherwise, as Fig. 6 in the main text.

S4 Metrics involved in determining the acoustic impedance misfit
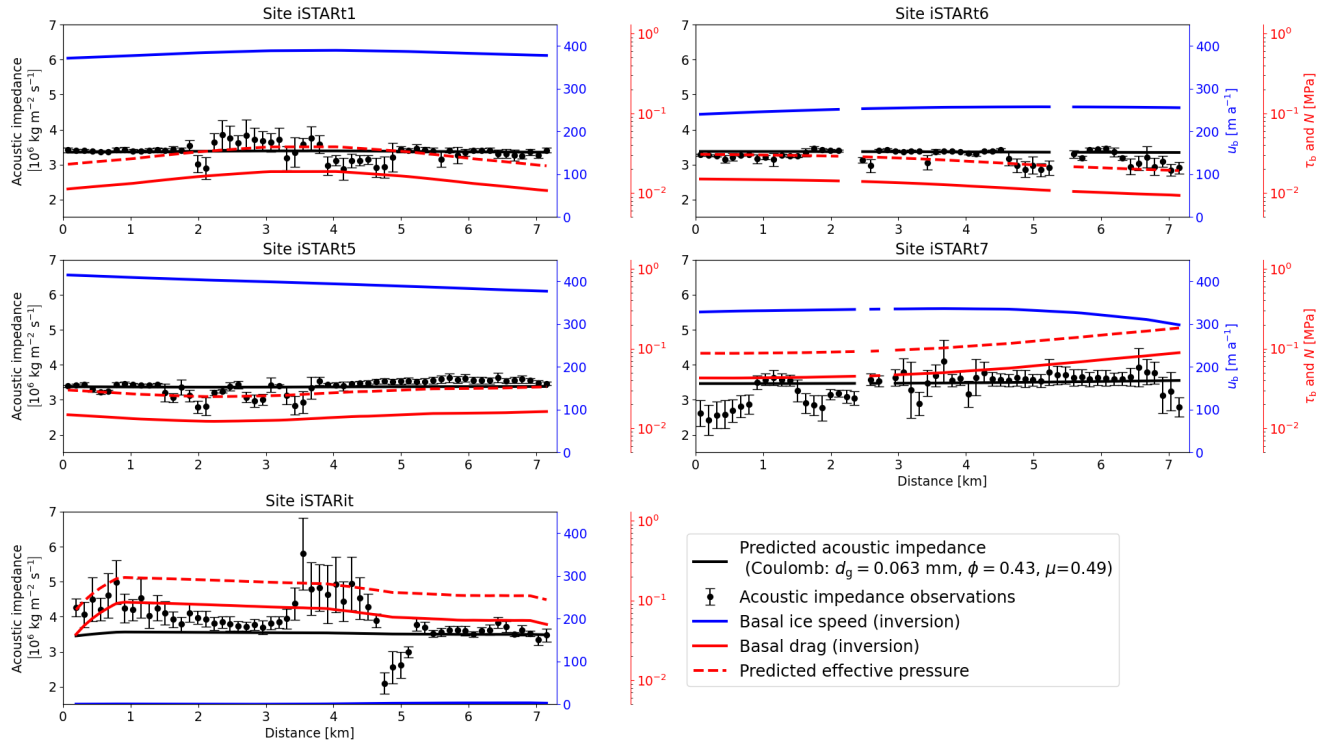
Figure S4. Metrics involved in predicting the acoustic impedance based on the Viscous Grain-Shearing (VGS) theory and calculating the misfit to the seismic observations. The black, blue, and red colours (lines, points, and axes) represent acoustic impedance, basal ice speed, and basal drag and effective pressure, respectively. The results are based on the Coulomb sliding law with the maximum a posteriori (MAP) parameter values.

5 S5 Incompatible $u_\mathrm{b}-\tau_\mathrm{b}$ pairs for small C_S values

When using the Schoof sliding law, C_S values smaller than $1 \cdot 10^3$ MPa m$^{-1/3}$ s$^{1/3}$ (e.g., $C_\mathrm{S} = 7.624$ MPa m$^{-1/3}$ s$^{1/3}$ suggested by Brondex et al., 2017) show a high percentage of incompatible (can not be explained by Eq. 7) $u_\mathrm{b}-\tau_\mathrm{b}$ pairs, inhibiting the determination of a misfit (Fig. S5, S15, and S16; see also Brondex et al., 2019). As this information is available prior to applying the Bayesian model selection, but was not used to constrain the C_S prior, we update $P(\Theta_i|M_i)$ by incorporating the
10 information from the inverted $u_\mathrm{b}-\tau_\mathrm{b}$ using Bayes' rule (Eq. 19). However, the posterior probabilities without this normalization are shown in Fig. S6. Since the chosen parameter space Θ_i does not lead to incompatible $u_\mathrm{b}-\tau_\mathrm{b}$ pairs near the seismic data sites for any of the other sliding laws, their posterior probabilities are not affected. Note that their final normalized probabilities differ because of the change in the posterior probability of the Schoof sliding law.
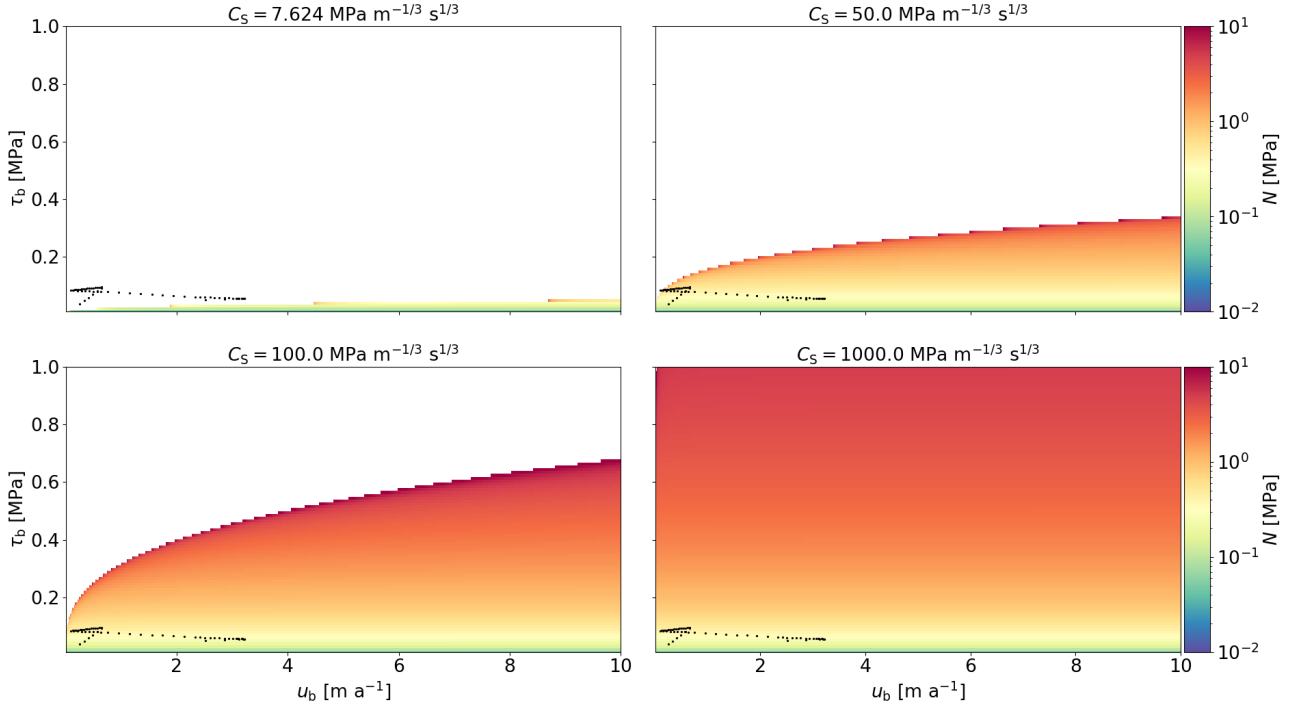
Figure S5. Simple toy experiment illustrating the $u_\mathrm{b}-\tau_\mathrm{b}$ pairs incompatible with Eq. 7 for different C_S values ($C_\mathrm{max} = 0.2$ and $m = 1/3$). Smaller C_S values, generally corresponding to smoother beds, lead to more incompatible $u_\mathrm{b}-\tau_\mathrm{b}$ pairs (larger white area). This issue primarily arises for small u_b and comparatively large τ_b values at site iSTARit located between two tributaries (black dots).
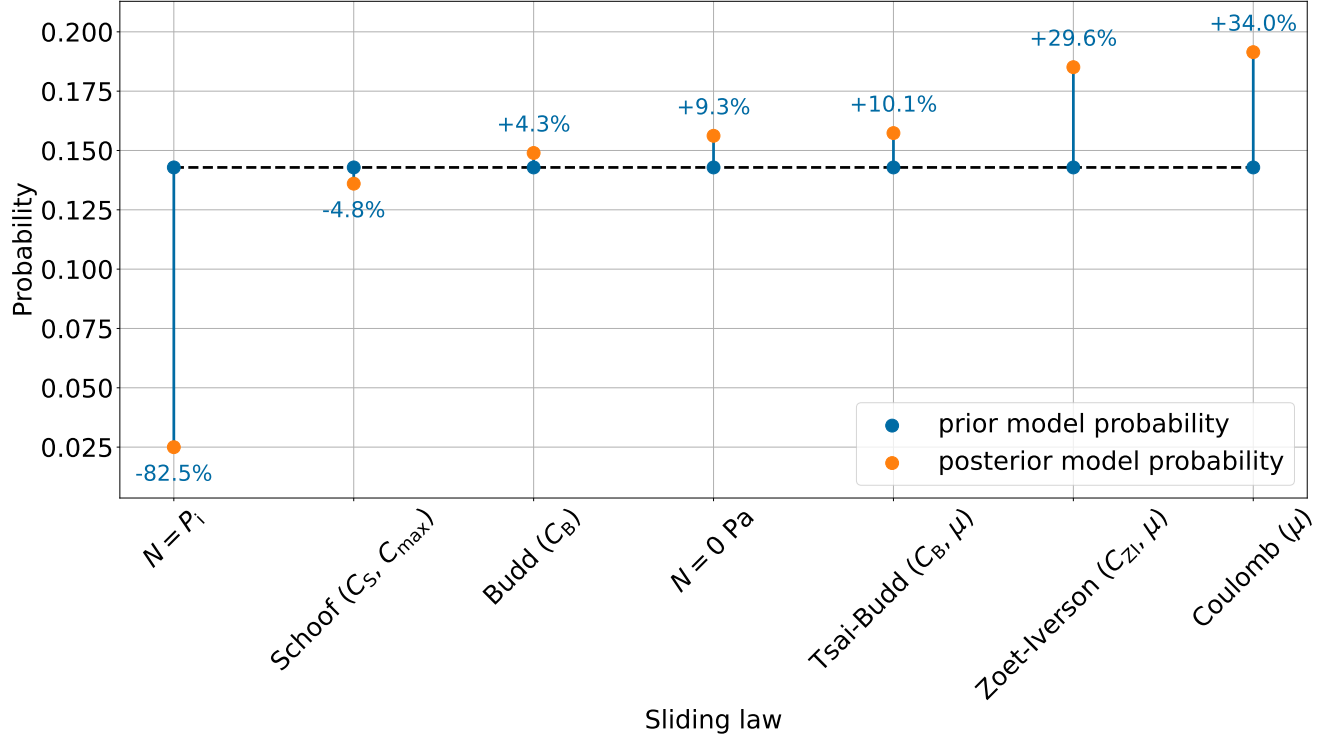
Figure S6. Normalized probabilities (Eq. 18) of all sliding laws examined in this study given the acoustic impedance observations collected on PIG. The prior model probability is taken as $P(M_i) = 1/n$, rather than $P(M_i|I) = 1/n$, and consequently, no normalization via $P(I|M_i)$ (Eq. 19) is applied. This leads to a significant reduction in the posterior probability of the Schoof sliding law due to an increasing number of incompatible $u_b - \tau_b$ pairs for C_S values smaller than $1 \cdot 10^3$ MPa m$^{-1/3}$ s$^{1/3}$ (see Fig. S5 for a simple toy experiment), resulting in overall 27 % of the likelihood being undefined (NaN), which is treated as zero likelihood here. Otherwise, as Fig. 6 in the main text.

S6 Prior distribution

S6.1 Porosity and grain diameter

Site	Porosity [%]	Clay [%]	Silt [%]	Sand [%]	Gravel [%]	Facies	Notes
BEAMISH	35	8	36	30	27	ST	Recovered from beneath Rutford Ice Stream (Smith, unpublished data)
PIGA	36	30	31	26	13	IT	Recovered from PIG ice shelf (Smith et al., 2017)
PIGB	39	28	28	33	11	IT	Recovered from PIG ice shelf (Smith et al., 2017)
VC415	34	3	46	36	14	ST	Deposited seaward of Dotson Ice Shelf during the Last Glacial Maximum (Smith et al., 2011)
VC417	35	3	51	37	8	ST	Deposited seaward of Dotson Ice Shelf during the Last Glacial Maximum (Smith et al., 2011)

Table S1. Porosity and grain diameter data used to determine the corresponding prior distributions. The facies are ice tranistional sediment deposited at or close to the grounding line (IT) and subglacial till deposited at the base of the ice stream (deformation till; ST).

S6.2 Maximum up-slope angle of the bed and Iken's bound

The distribution of the up-slope angles of the bed in flow direction (β) and the corresponding Iken's bound ($C_{\max} = \tan\beta$; Fig. S7) is examined for the center part of Pine Island Glacier (PIG; magenta box in Fig. S8). As the horizontal grid resolution of Bedmap2 is 1 km (Fretwell et al., 2013), the maximum up-slope angle (and therefore $C_{\max}$) on smaller scales might be significantly steeper than suggested by the distribution in Fig. S7. For example, autonomous underwater vehicle (AUV) data collected downstream of Thwaites Glacier (1.5 m horizontal resolution; Graham et al., 2022) and under the Thwaites Eastern Ice Shelf (2 m horizontal resolution; Wåhlin, unpublished data) indicate that the maximum $C_{\max} > 0.7$ (largest value tested within this study; Fig. S9). ~~However, as the horizontal resolution of the inversion used to derive the basal shear stress and sliding speed is much coarser (1 km; same as the Bedmap2 resolution), it is not straightforward to determine the $C_{\max}$ prior directly from the AUV data . Nevertheless, the~~ As the bed roughness and therefore the actual relevant scale are unknown and likely vary spatially, the chosen $C_{\max}$ ~~prior aims to incorporate~~ prior incorporates the coarse resolution Bedmap2 data as a conservative lower bound and accounts for the higher bed angles observed at smaller scales through a more gradual decline towards higher values ~~while aligning the highest probability with the extreme values in Fig. S7.~~.

S7
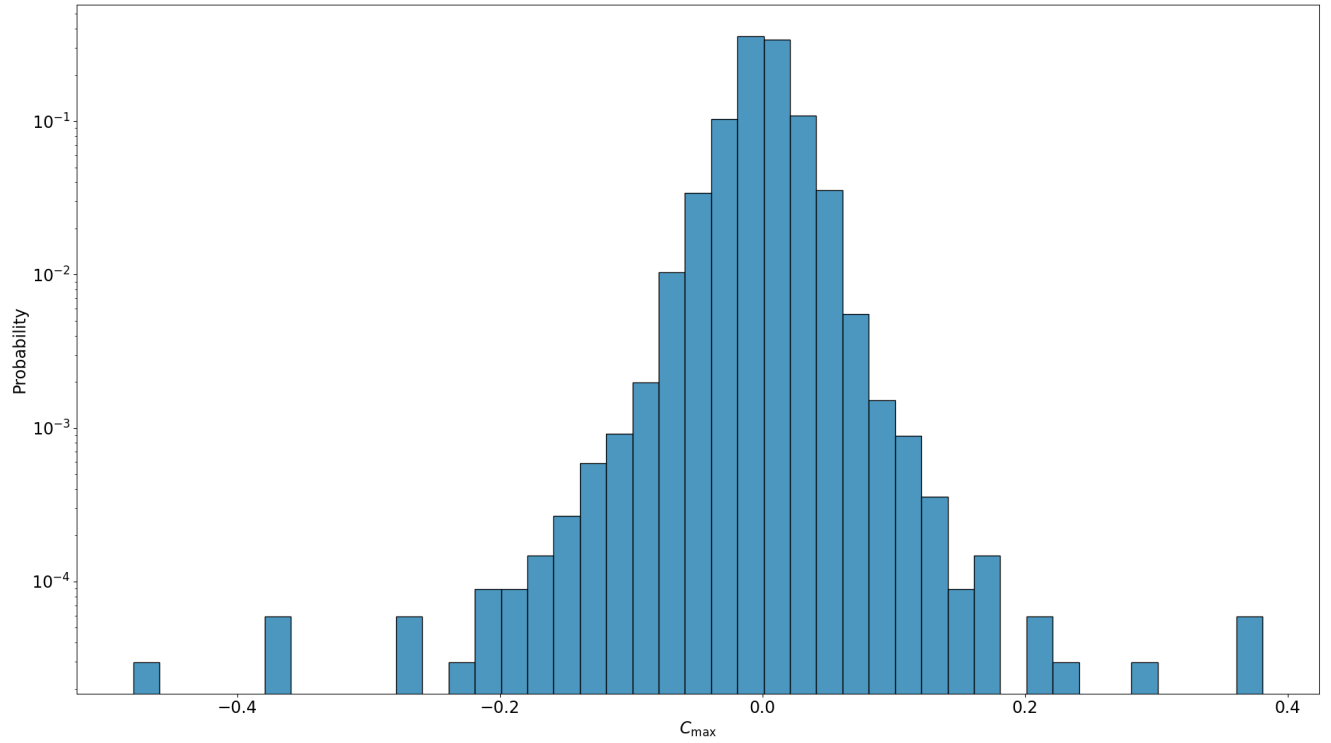
Figure S7. C_{max} estimation derived from the distribution of bed up-slope angles in flow direction within the magenta box in Fig. S8. The Bedmap2 horizontal grid resolution is 1 km (Fretwell et al., 2013). The bin width is 0.02.
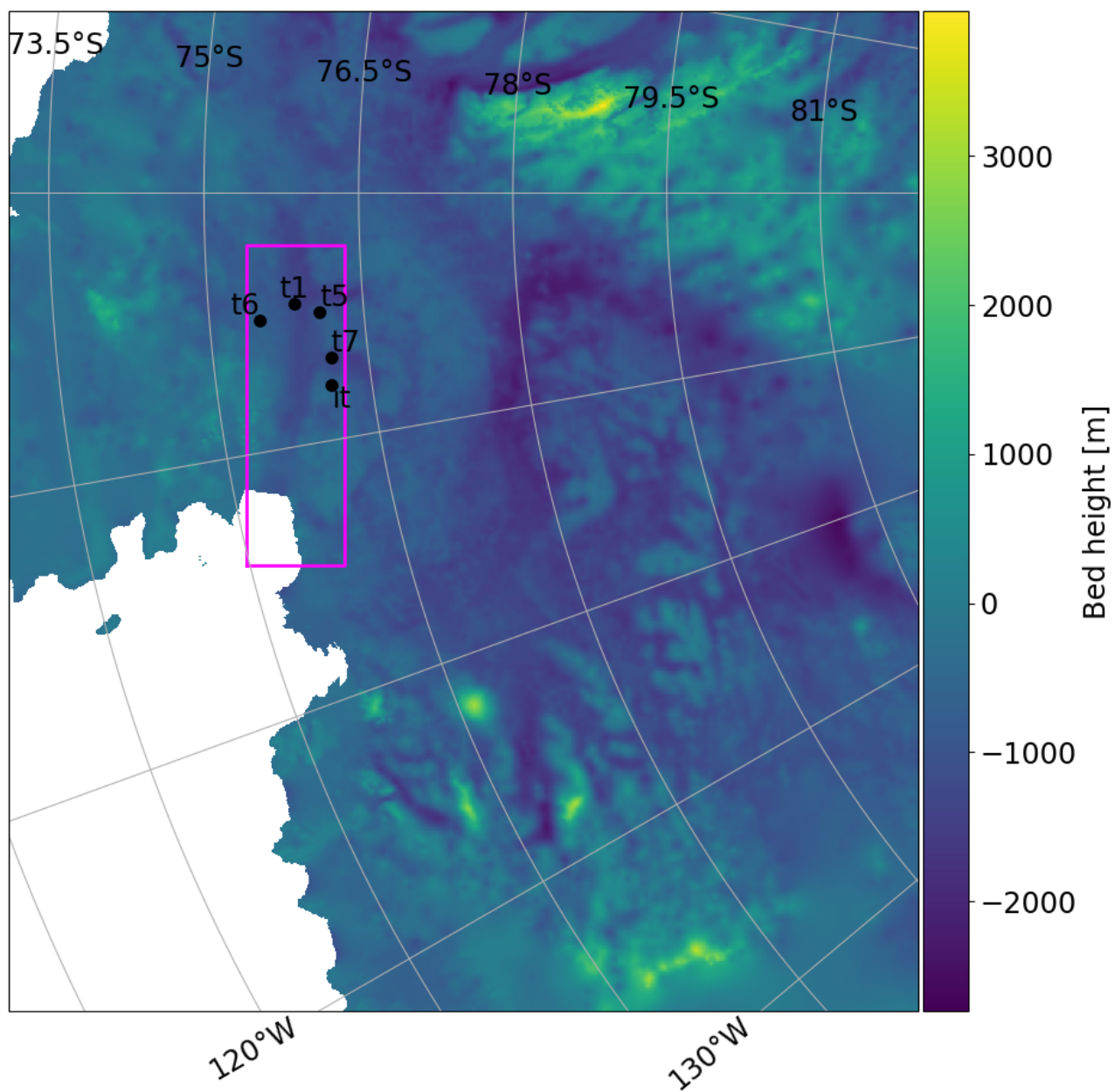
Figure S8. Bed height for areas with ice cover (grounded and floating; based on Bedmap2; Fretwell et al., 2013). The magenta box frames the main trunk of Pine Island Glacier (PIG) and the black dots mark the locations of the acoustic impedance data sites.
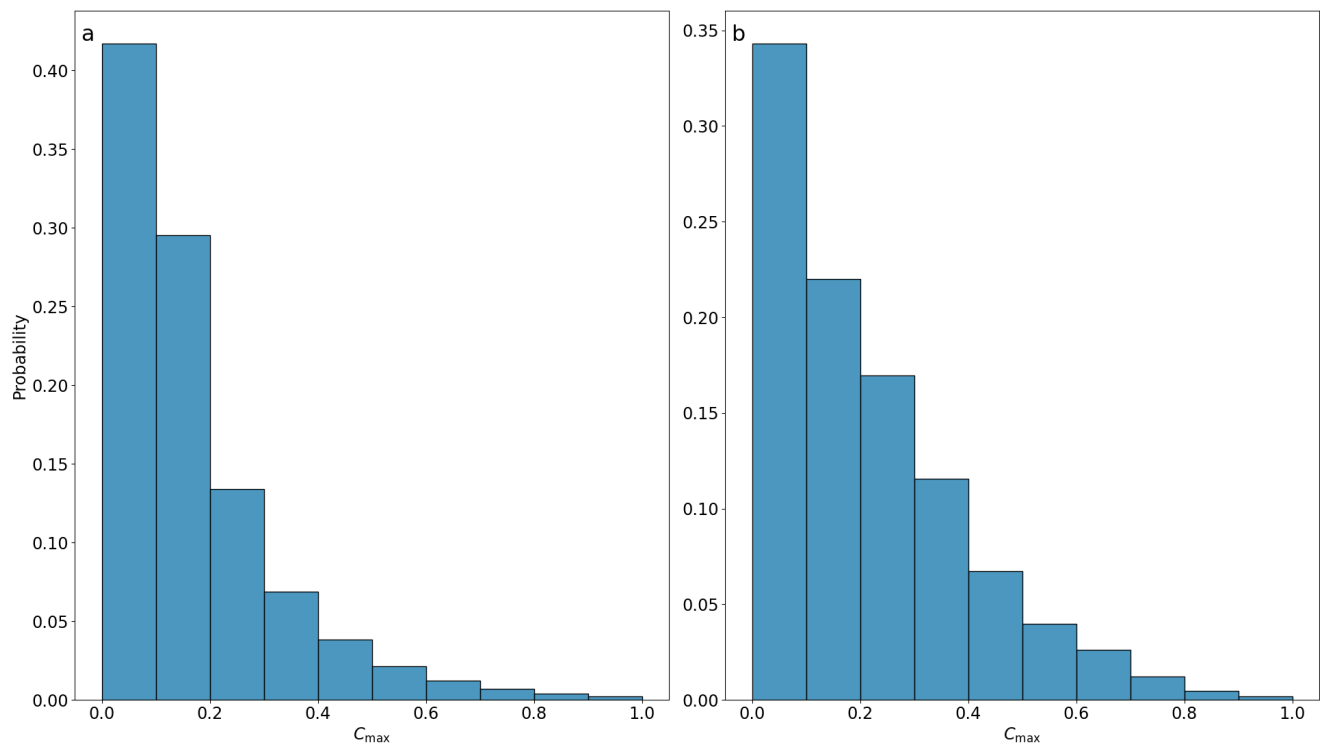
Figure S9. C_{max} estimation derived from the distribution of bed slope angles from autonomous underwater vehicle (AUV) data collected downstream of Thwaites Glacier (a; 1.5 m horizontal resolution; Graham et al., 2022) and under the Thwaites Eastern Ice Shelf (b; 2 m horizontal resolution; Wåhlin, unpublished data). The bin width is 0.1. C_{max} values > 1.0 are not shown here. The corresponding spatial distributions are shown in Fig. S10.
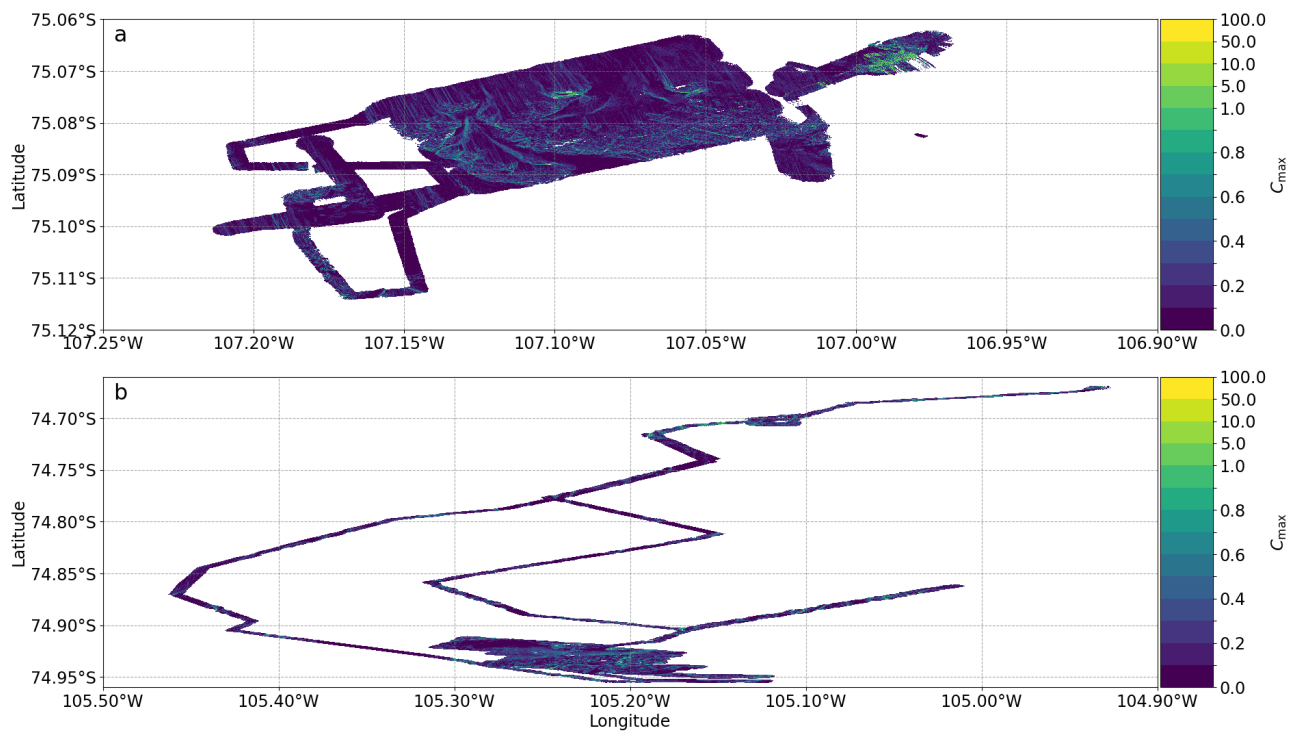
Figure S10. Spatial distribution of the autonomous underwater vehicle (AUV) data shown in Fig. S9. Note the change in colorbar step at $C_{\max} = 1.0$.

S7 Acoustic impedance data-model misfit under different sliding laws (maximum 3D)

 ### S7.1 Fixed effective pressure endmember scenarios $N = 0$ Pa and $N = p_{\mathrm{i}}$
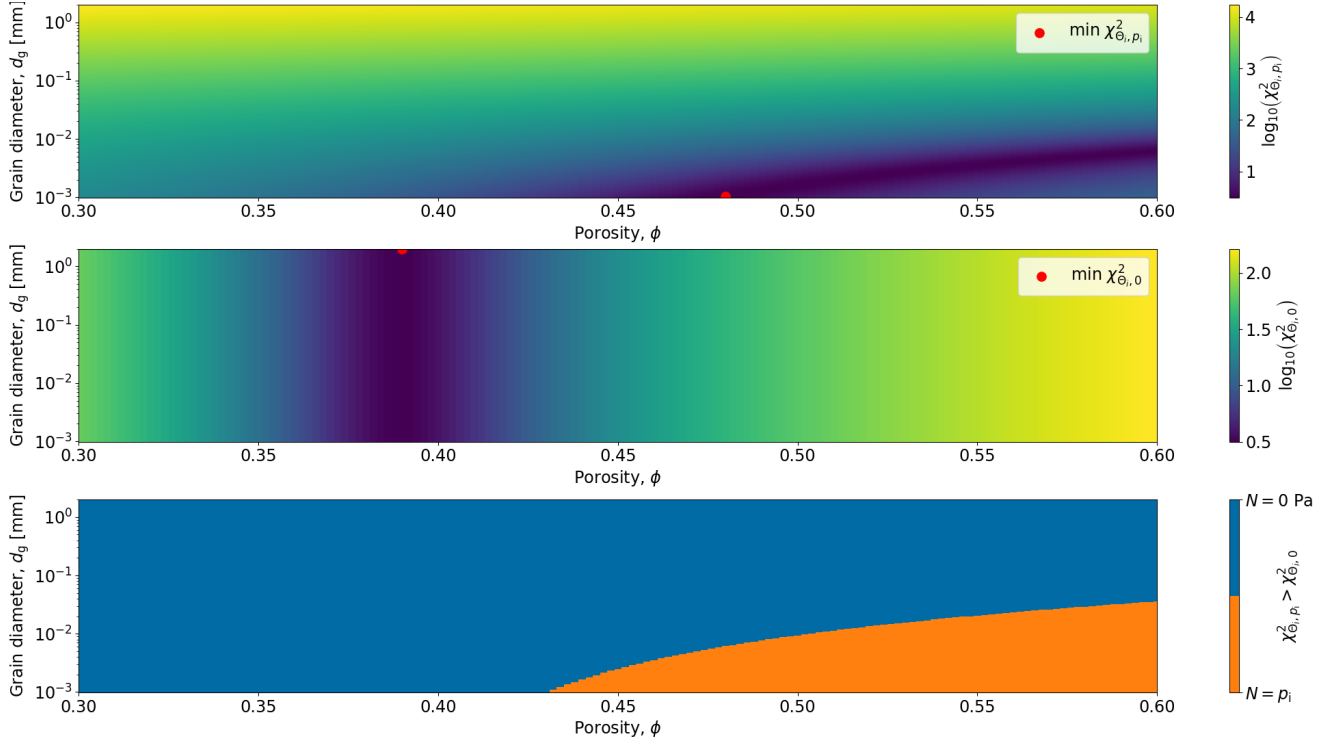
Figure S11. Variations of the misfit $\chi^2_{\Theta_i}$ with the two model parameters grain diameter (d_{g}) and porosity (ϕ) under the fixed effective pressure endmember scenarios $N = p_{\mathrm{i}}$ (top panel) and $N = 0$ Pa (center panel). The bottom panel shows the preferred endmember scenario within the parameter space. The red dots mark the minimum misfit.

S7.2 Budd (C_B)
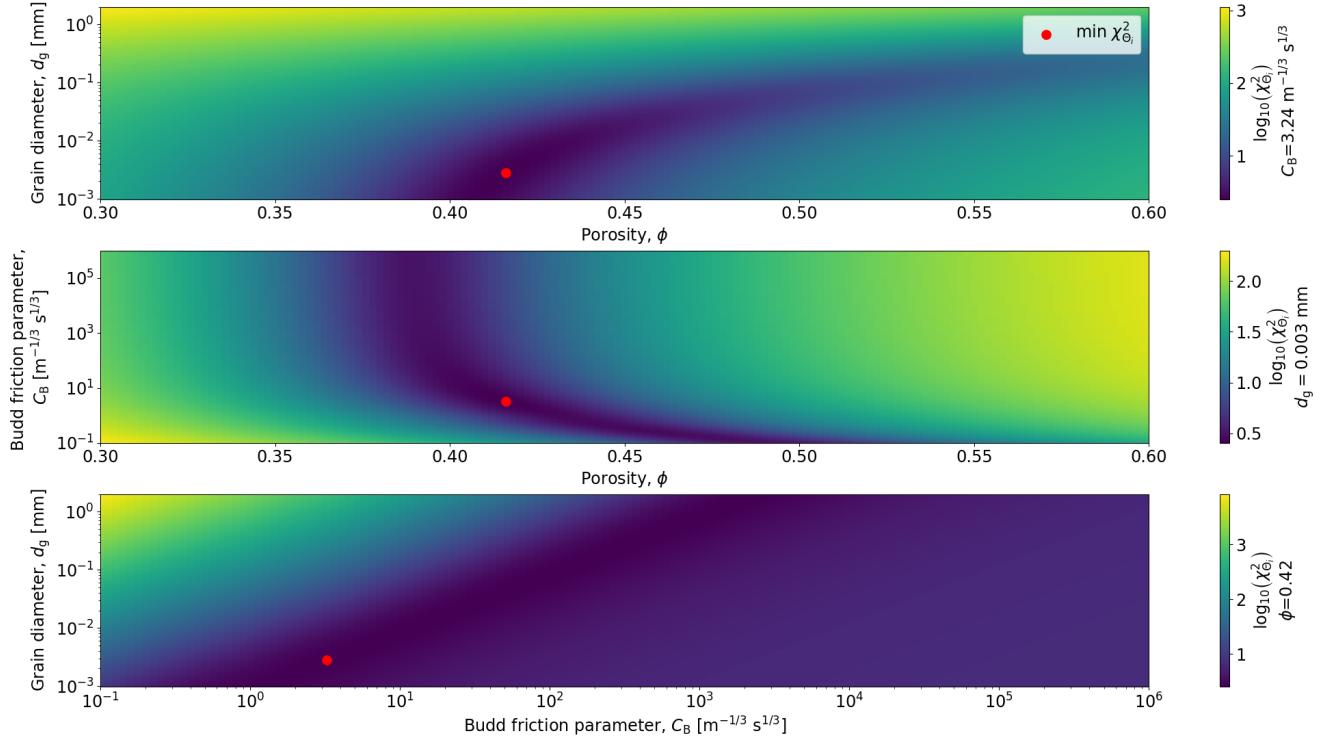
Figure S12. Variations of the misfit $\chi^2_{\Theta_i}$ with the three model parameters grain diameter (d_g), porosity (ϕ), and Budd friction parameter (C_B) under a Budd sliding law. For the parameter not shown, the value yielding the minimum misfit is used and denoted next to the colorbar of the corresponding panel. The red dots mark the minimum misfit.

S7.3 Tsai-Budd (C_B)
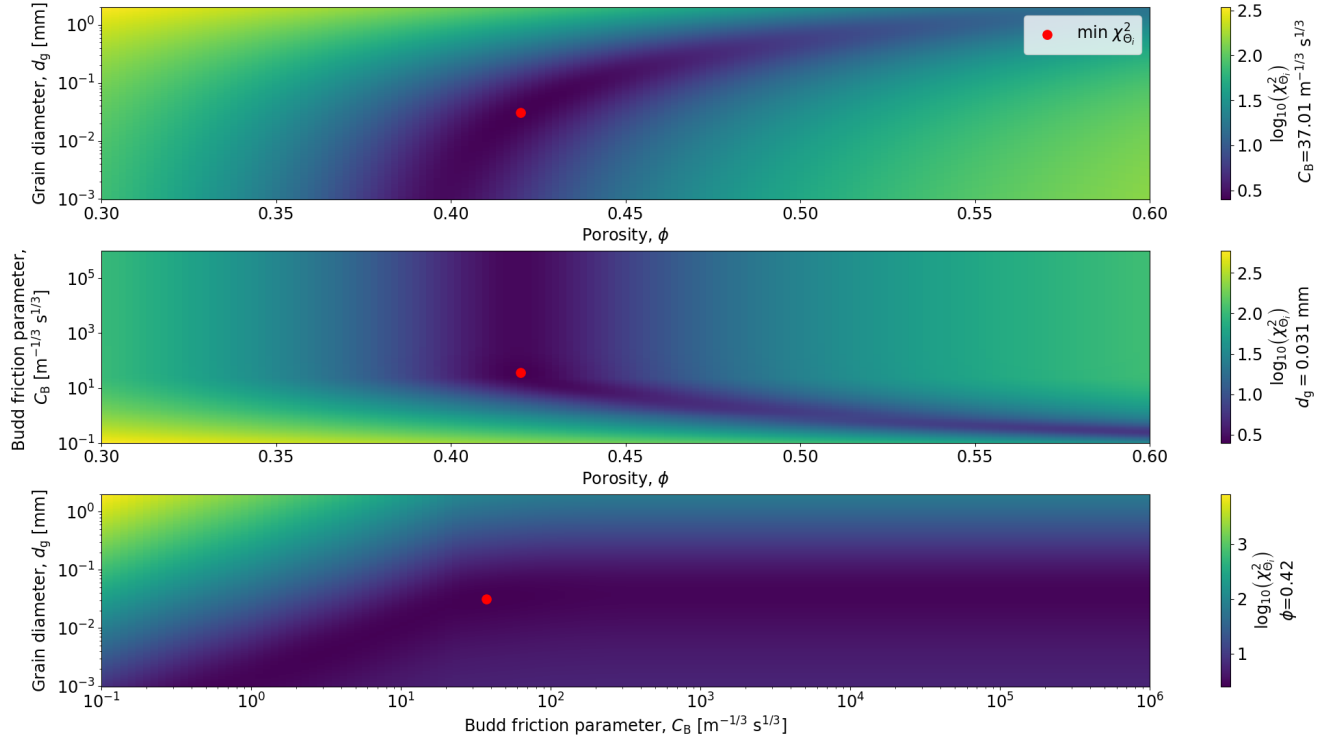
Figure S13. Variations of the misfit $\chi^2_{\Theta_i}$ with the three model parameters grain diameter (d_g), porosity (ϕ), and Budd friction parameter (C_B) under a Tsai-Budd sliding law (μ fixed at 0.5). Otherwise as Fig. S12.

S7.4 Tsai-Budd (μ)
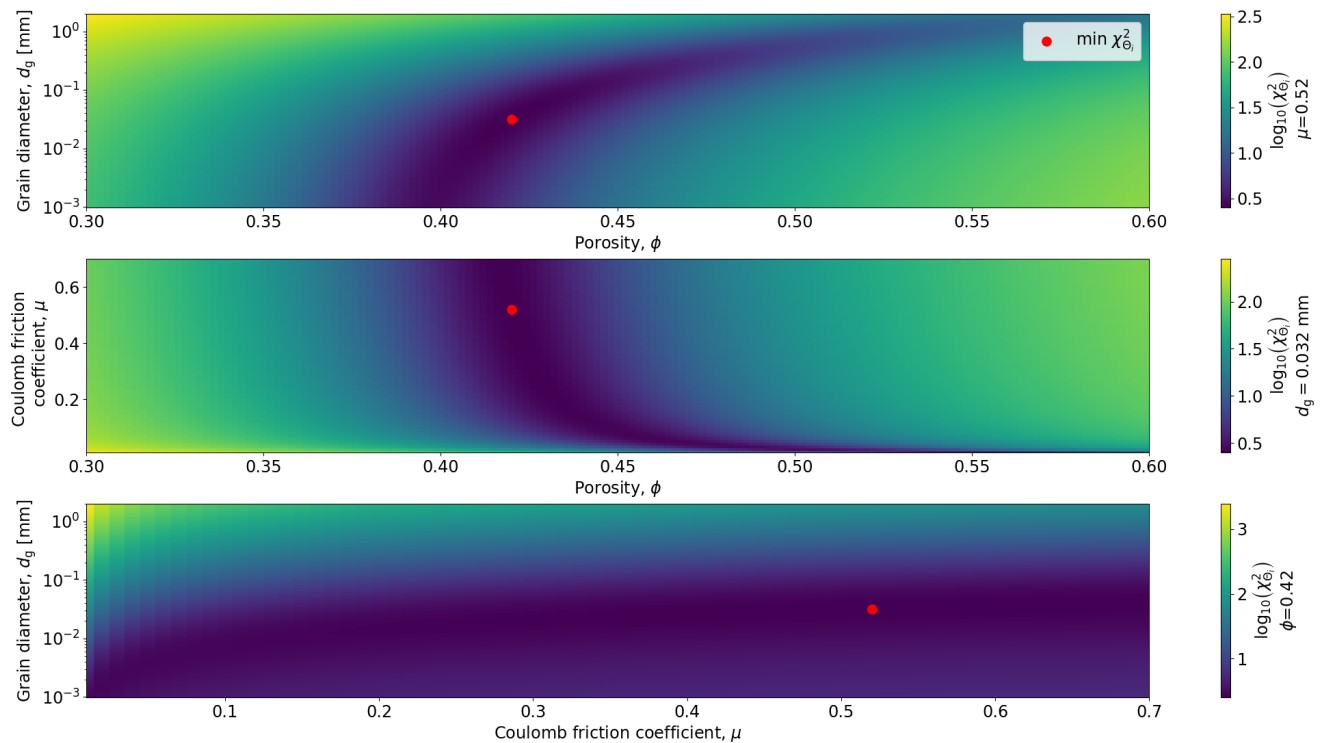
Figure S14. Variations of the misfit $\chi^2_{\Theta_i}$ with the three model parameters grain diameter (d_g), porosity (ϕ), and Coulomb friction coefficient (μ) under a Tsai-Budd sliding law (C_B fixed at $37.01 \text{ m}^{-1/3} \text{ s}^{1/3}$). Otherwise as Fig. S12.
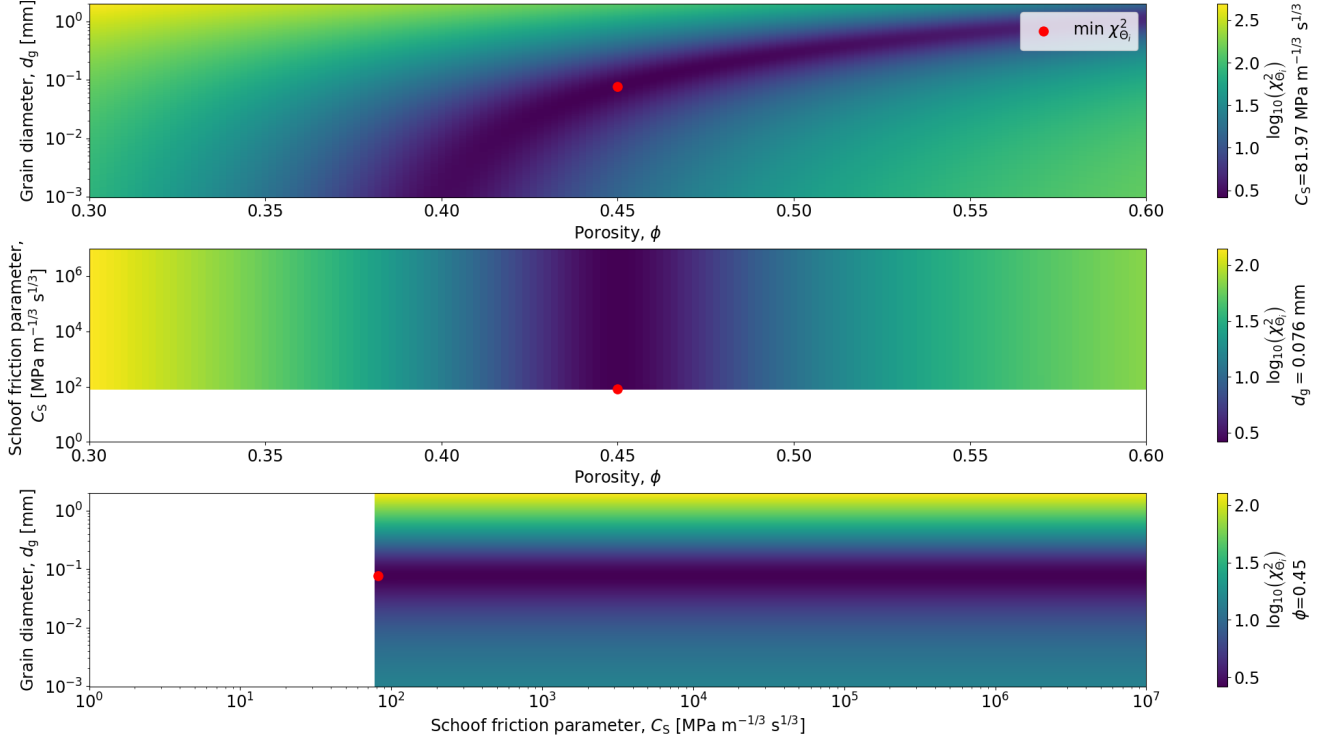
Figure S15. Variations of the misfit $\chi^2_{\Theta_i}$ with the three model parameters grain diameter (d_{g}), porosity (ϕ), and Schoof friction parameter (C_{S}) under a Schoof sliding law (C_{max} fixed at 0.2). The determination of $\chi^2_{\Theta_i}$ is only possible when the number of incompatible $u_{\mathrm{b}} - \tau_{\mathrm{b}}$ pairs is small (Sec. S5 and Fig. S16). Otherwise as Fig. S12.
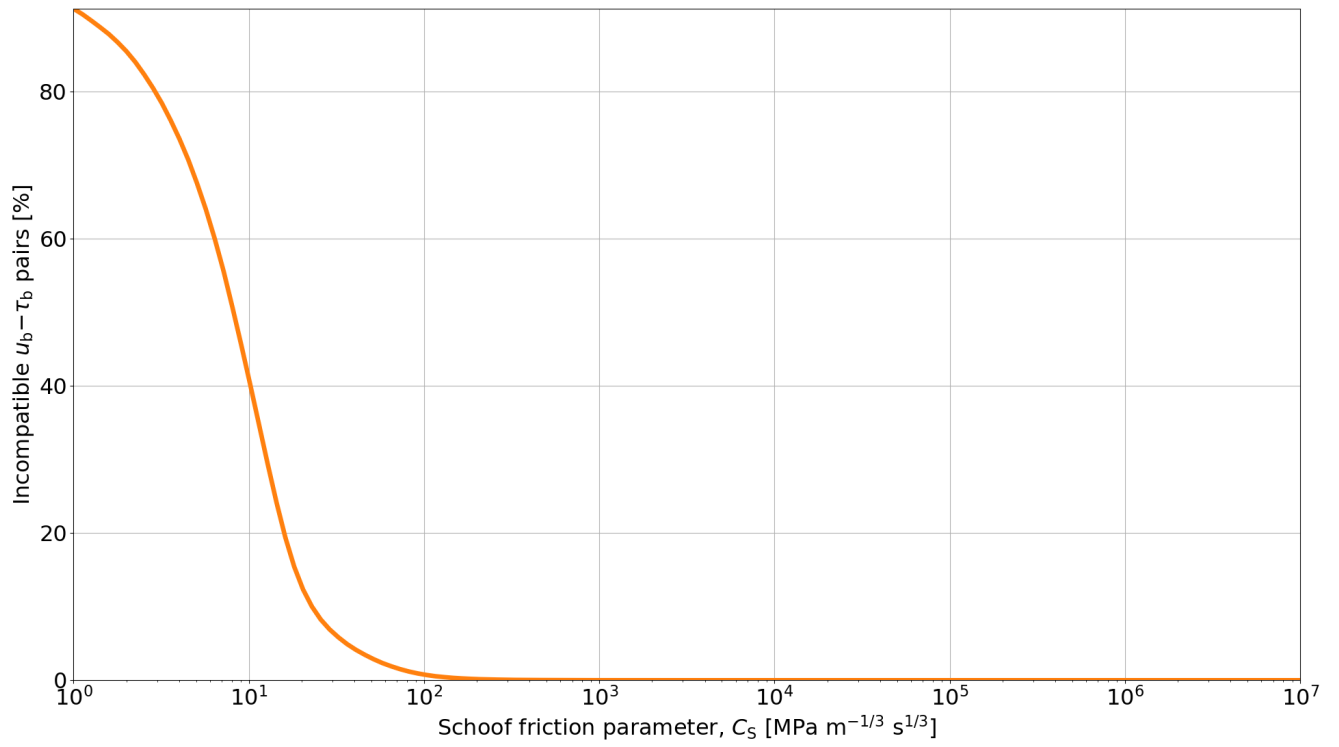
Figure S16. Percentage of incompatible $u_{\mathrm{b}}-\tau_{\mathrm{b}}$ pairs under a Schoof sliding law when varying the Schoof friction parameter (C_{S}; C_{max} fixed at 0.2).
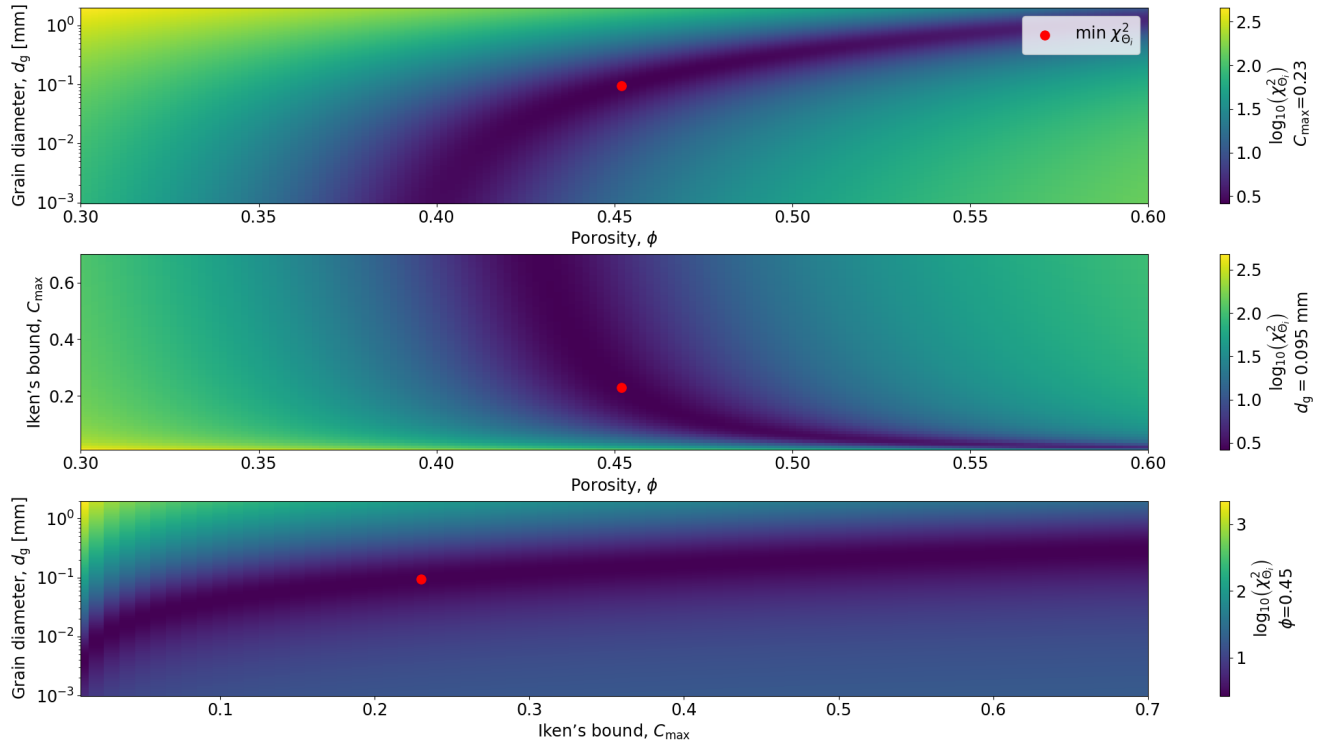
Figure S17. Variations of the misfit $\chi^2_{\Theta_i}$ with the three model parameters grain diameter (d_{g}), porosity (ϕ), and Iken's bound (C_{max}) under a Schoof sliding law (C_{S} fixed at $1 \cdot 10^3$ MPa m$^{-1/3}$ s$^{1/3}$; Sec. S5). Otherwise as Fig. S12.
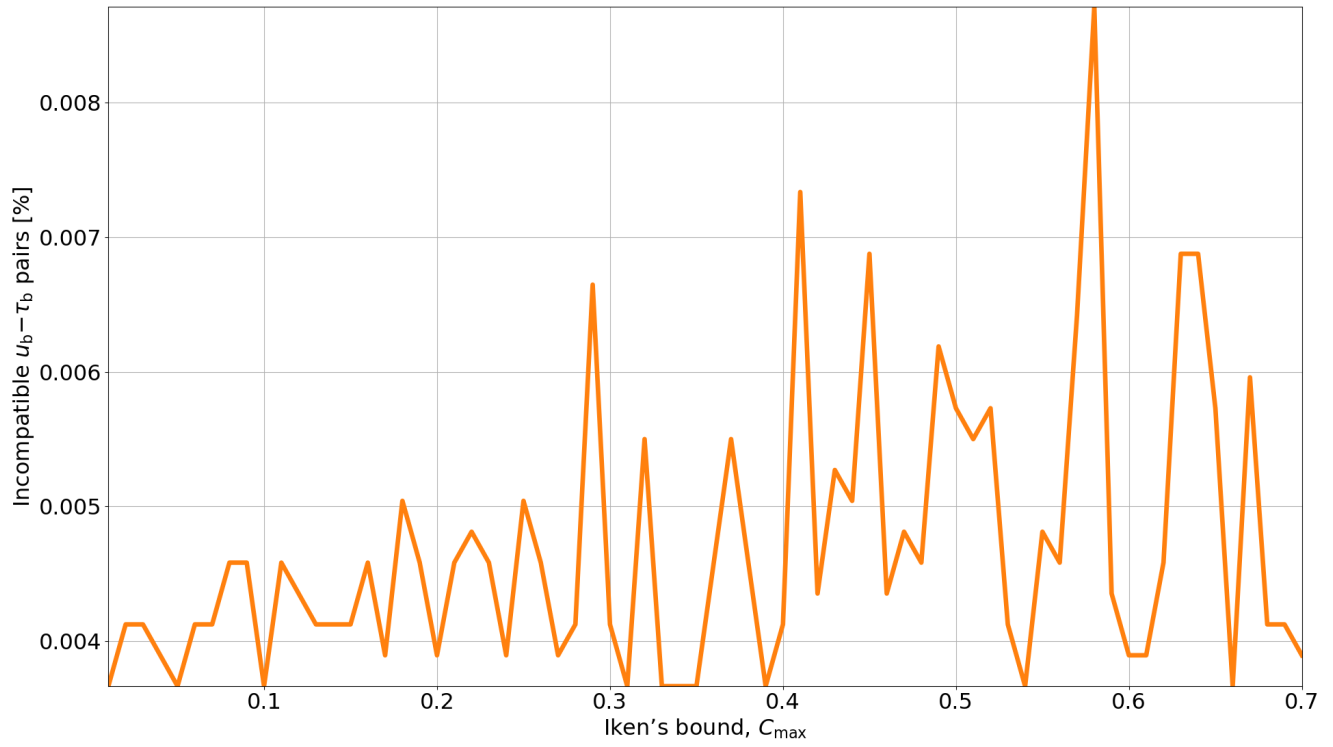
Figure S18. Percentage of incompatible $u_{\mathrm{b}}-\tau_{\mathrm{b}}$ pairs under a Schoof sliding law when varying Iken's bound ($C_{\max}$; C_{S} fixed at $1 \cdot 10^3 \, \mathrm{MPa} \, \mathrm{m}^{-1/3} \, \mathrm{s}^{1/3}$; Sec. S5).

S7.7 Zoet-Iverson (μ)
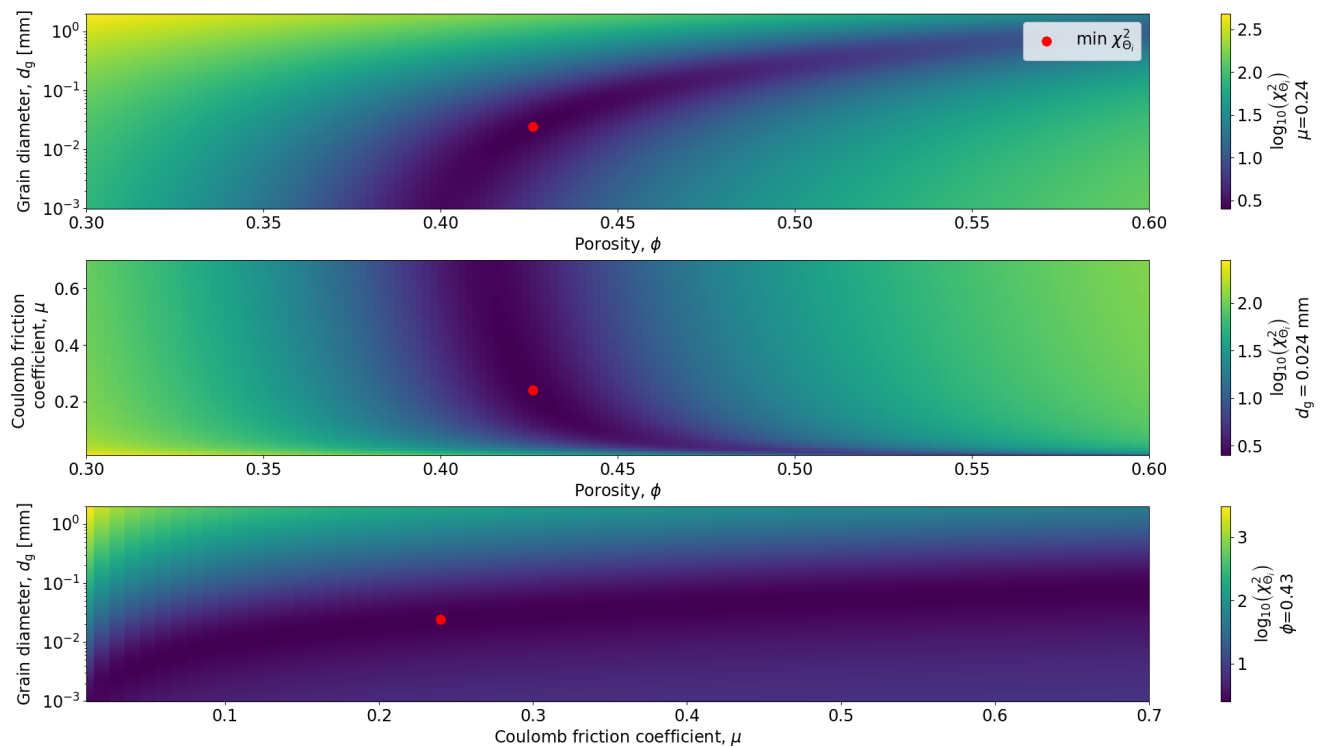
Figure S19. Variations of the misfit $\chi^2_{\Theta_i}$ with the three model parameters grain diameter (d_g), porosity (ϕ), and Coulomb friction coefficient (μ) under a Zoet-Iverson sliding law (C_ZI fixed at $\sim 340\ \mathrm{MPa}^{-1}\ \mathrm{m}\ \mathrm{a}^{-1}$). Otherwise as Fig. S12.
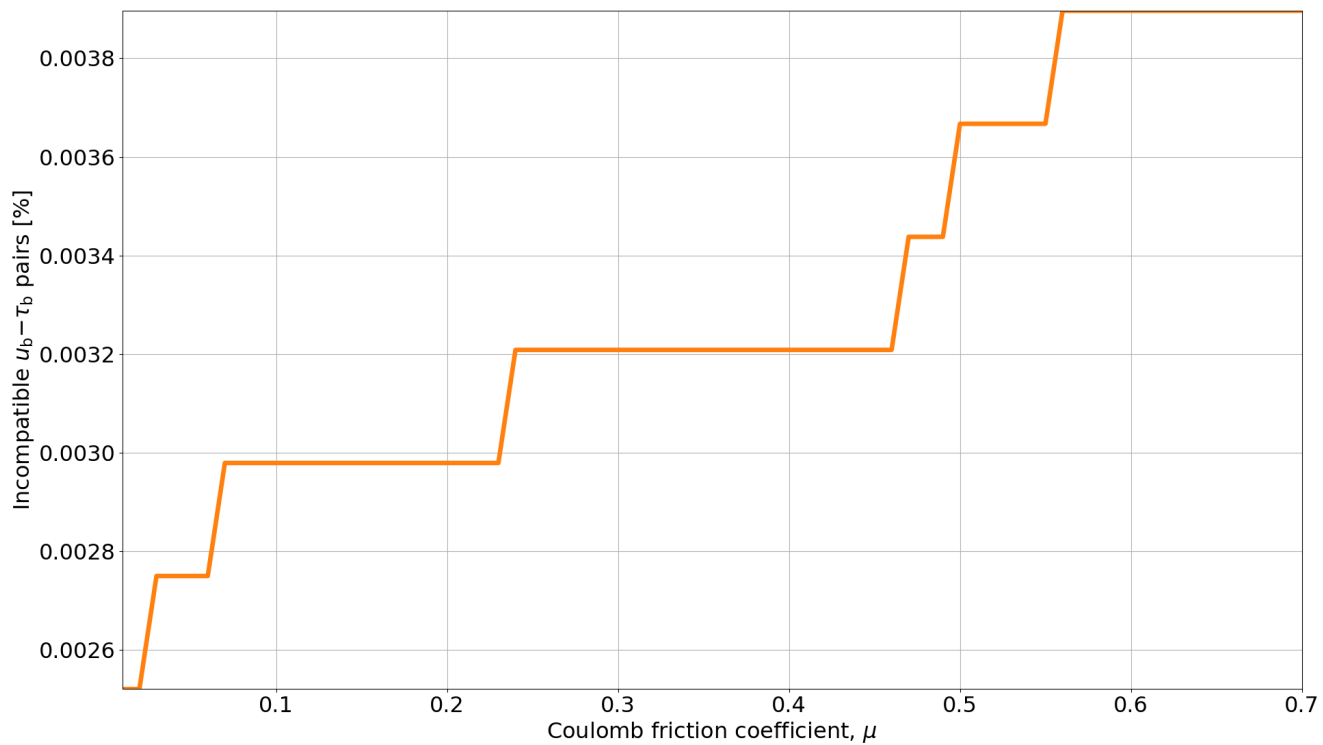
Figure S20. Percentage of incompatible $u_b - \tau_b$ pairs under a Zoet-Iverson sliding law when varying the Coulomb friction coefficient (μ; C_{ZI} fixed at ~ 340 MPa^{-1} m a^{-1}).

S7.8 Zoet-Iverson (C_{ZI})
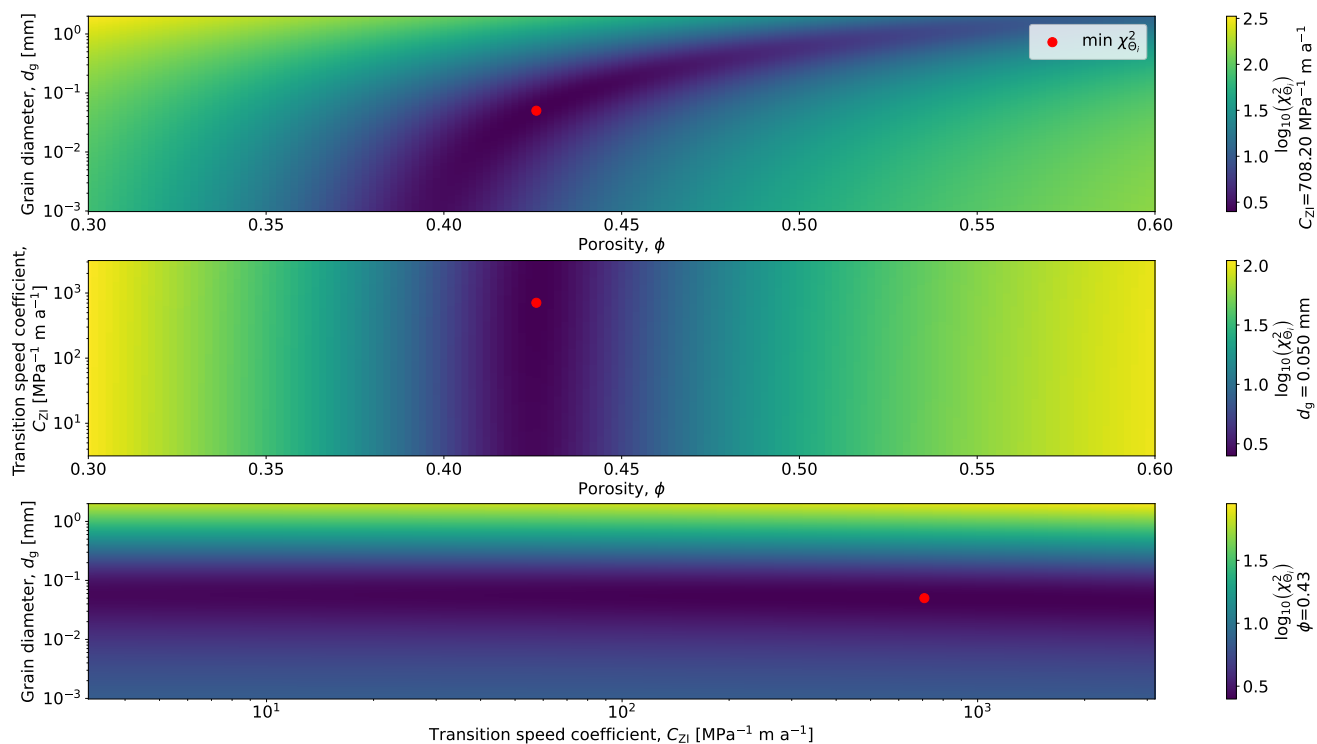
Figure S21. Variations of the misfit $\chi^2_{\Theta_i}$ with the three model parameters grain diameter (d_g), porosity (ϕ), and transition speed coefficient (C_{ZI}) under a Zoet-Iverson sliding law (Coulomb friction coefficient μ fixed at 0.5). Otherwise as Fig. S12.
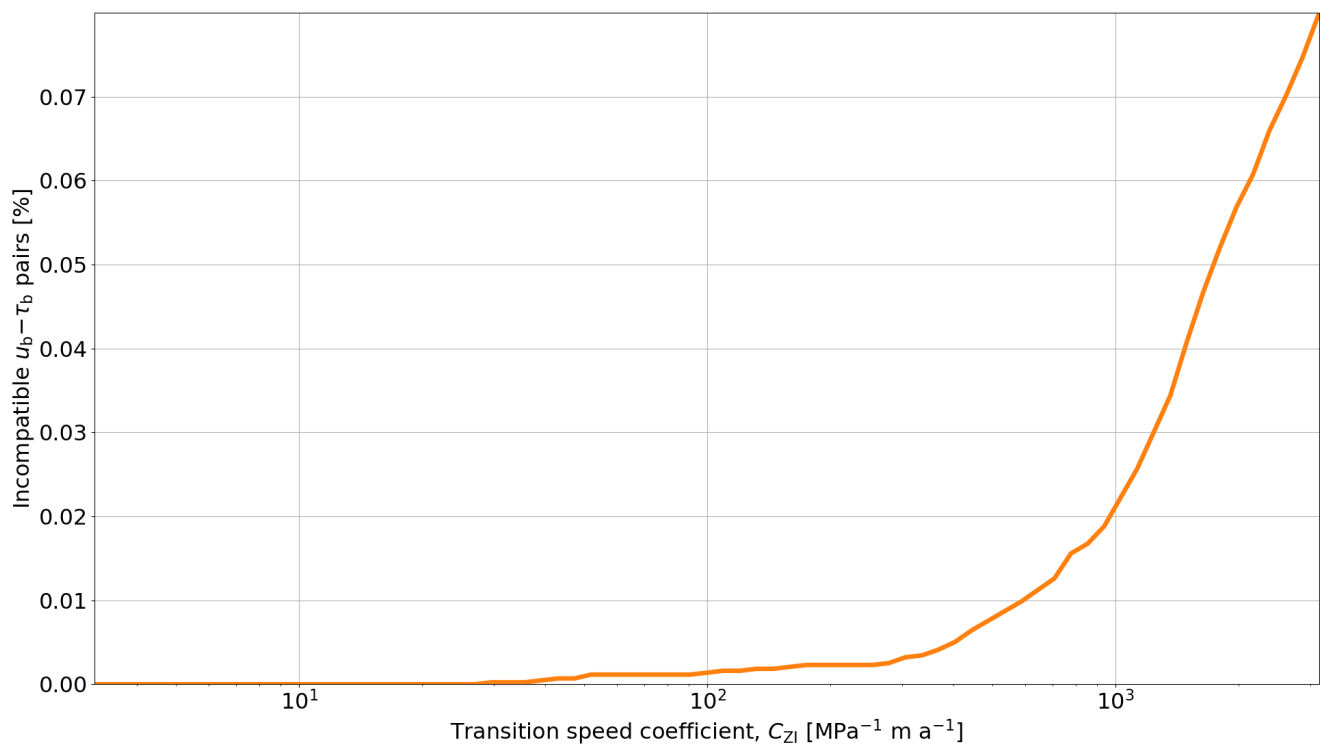
Figure S22. Percentage of incompatible $u_b-\tau_b$ pairs under a Zoet-Iverson sliding law when varying the transition speed coefficient (C_{ZI}; μ fixed at 0.5).

S8 Posterior probabilities when using different fractions of the overburden pressure
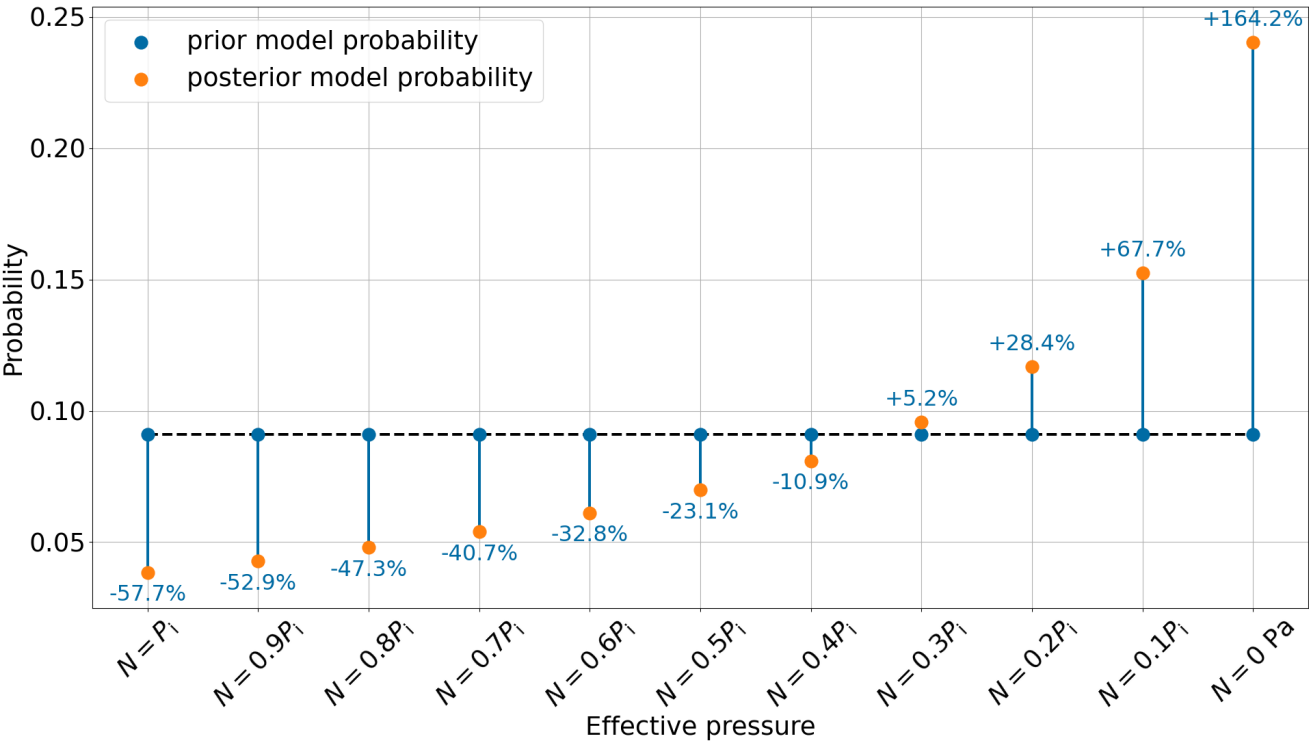
Figure S23. Normalized probabilities (Eq. 20) given the seismic observations collected on PIG when using different fractions of the overburden pressure, including the two endmember scenarios ($N = 0$ Pa and $N = p_i$). Otherwise, as Fig. 6 in the main text.

S9   Acoustic impedance for most probable parameters
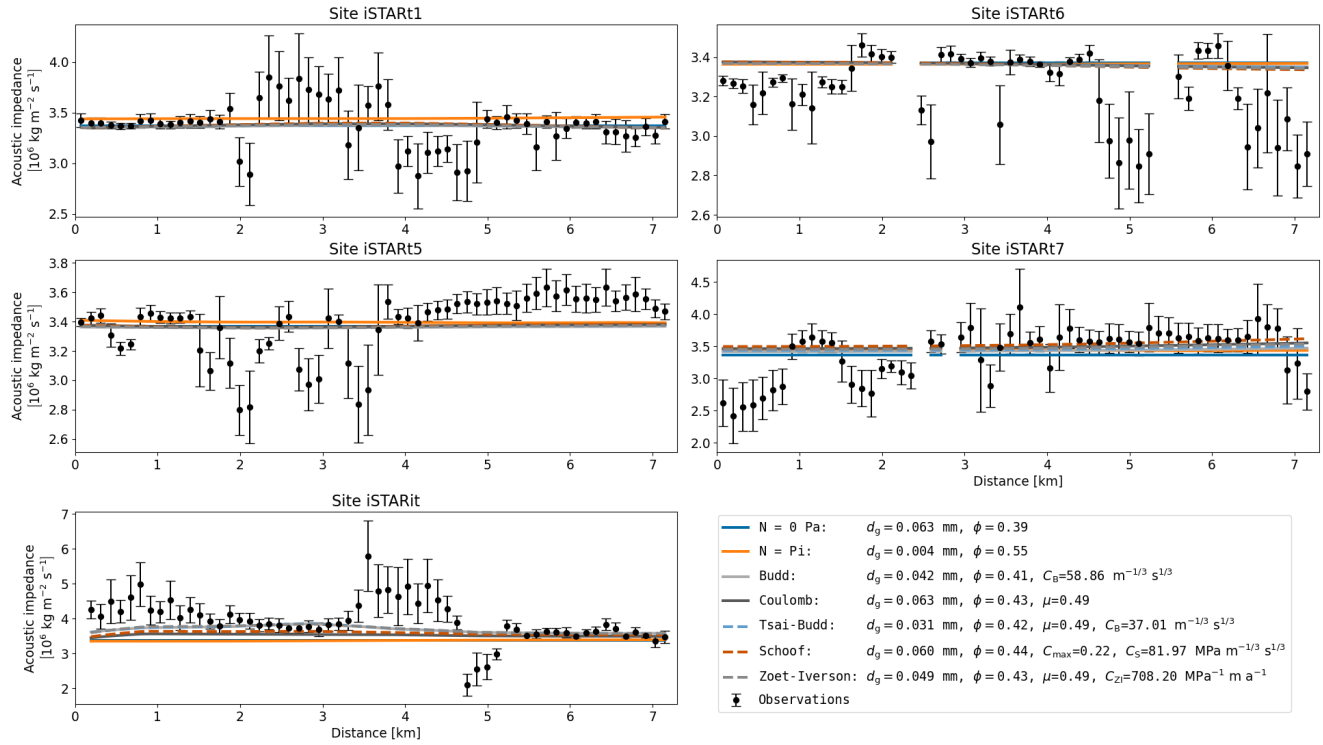
Figure S24. The different panels show the predicted acoustic impedance at the five data sites. For all sliding laws, the acoustic impedance curve is based on the MAP (highest posterior probability) model parameters shown in the legend.
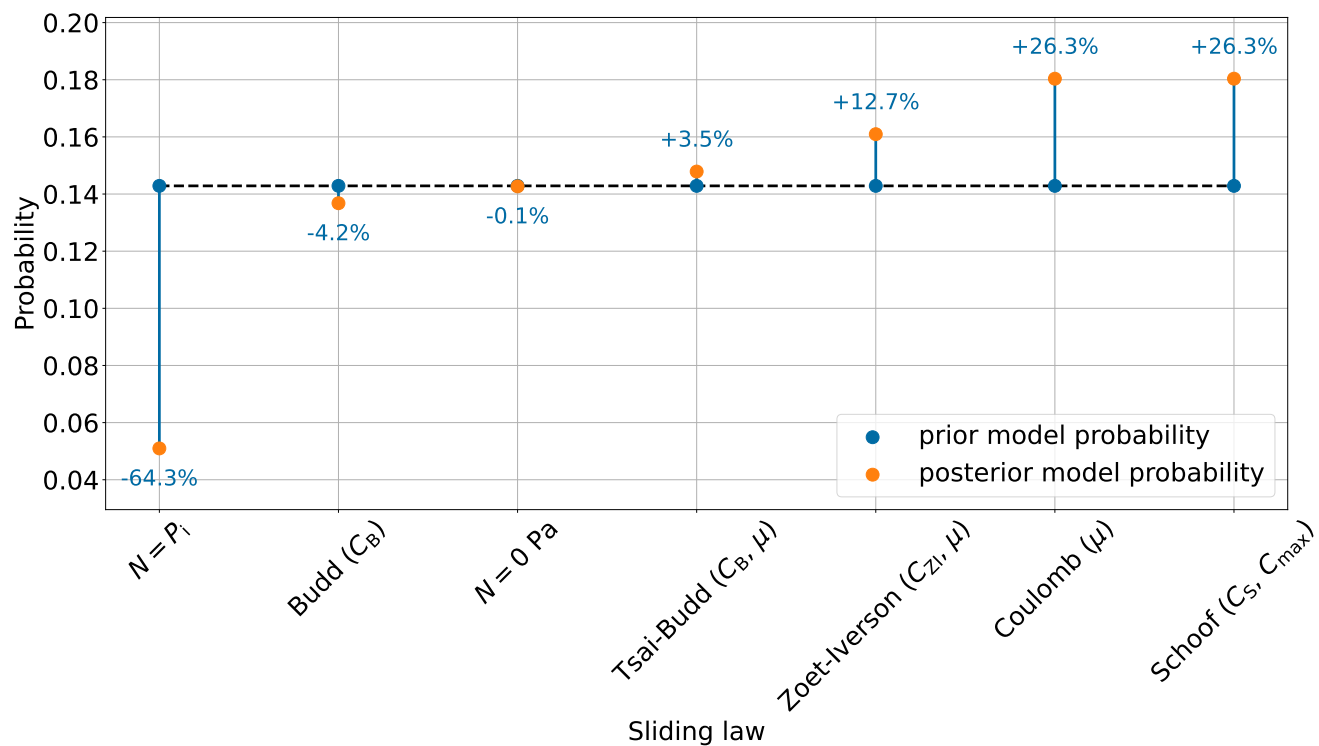
Figure S25. Normalized probabilities (Eq. 20) of all sliding laws examined in this study given the acoustic impedance observations collected on PIG, and log-uniform prior distributions for scaling coefficients and uniform priors for other parameters. Otherwise, as Fig. 6 in the main text.

S11 Effective pressure for most probable parameters
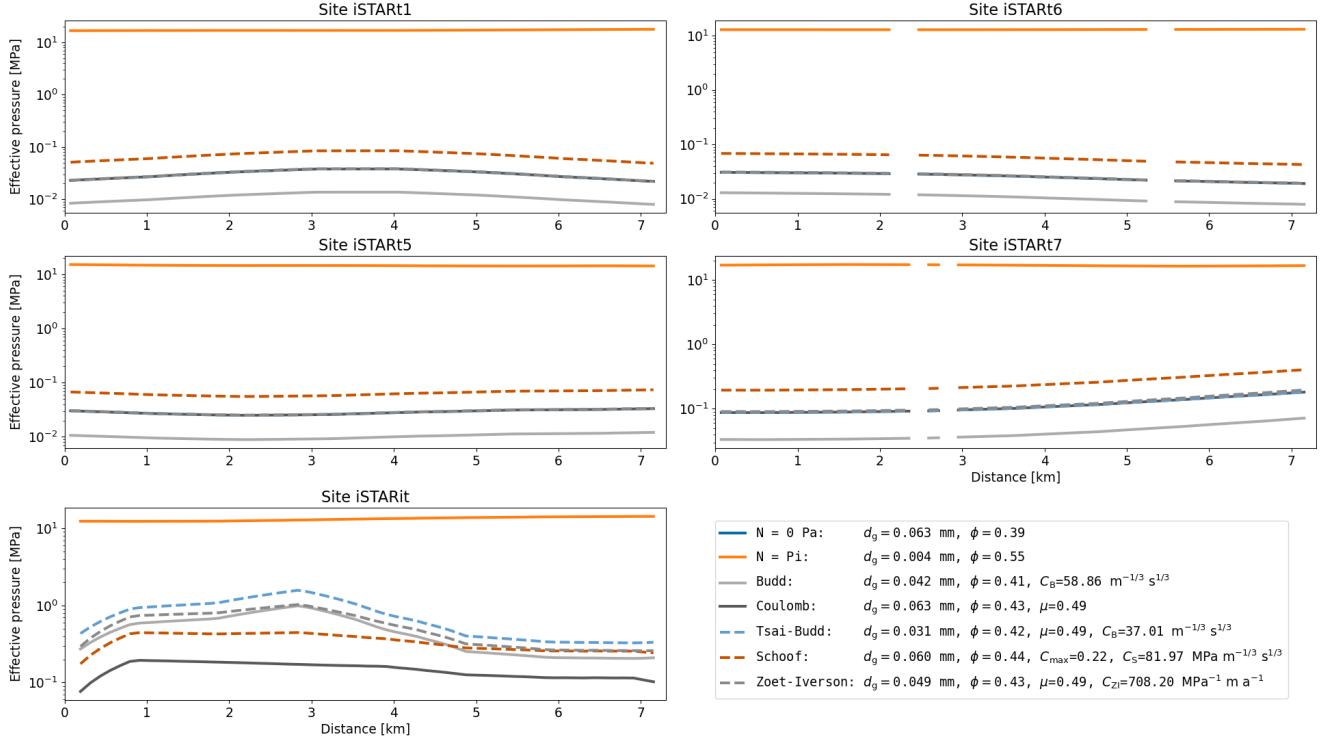
Figure S26. The different panels show the predicted effective pressure at the five data sites. For all sliding laws, the effective pressure curve is based on the MAP (highest posterior probability) model parameters. By definition, the low effective pressure endmember scenario has $N = 0$ Pa and only the MAP parameter values are shown here (not the curve itself). Note the logarithmic scale of the y-axes.

References

Brondex, J., Gagliardini, O., Gillet-Chaulet, F., and Durand, G.: Sensitivity of grounding line dynamics to the choice of the friction law, Journal of Glaciology, 63, 854–866, https://doi.org/10.1017/jog.2017.51, 2017.

45   Brondex, J., Gillet-Chaulet, F., and Gagliardini, O.: Sensitivity of centennial mass loss projections of the Amundsen basin to the friction law, The Cryosphere, 13, 177–195, https://doi.org/10.5194/tc-13-177-2019, 2019.

Fretwell, P., Pritchard, H. D., Vaughan, D. G., Bamber, J. L., Barrand, N. E., Bell, R., Bianchi, C., Bingham, R. G., Blankenship, D. D., Casassa, G., Catania, G., Callens, D., Conway, H., Cook, A. J., Corr, H. F., Damaske, D., Damm, V., Ferraccioli, F., Forsberg, R., Fujita, S., Gim, Y., Gogineni, P., Griggs, J. A., Hindmarsh, R. C., Holmlund, P., Holt, J. W., Jacobel, R. W., Jenkins, A., Jokat, W., Jordan, T., King,

50   E. C., Kohler, J., Krabill, W., Riger-Kusk, M., Langley, K. A., Leitchenkov, G., Leuschen, C., Luyendyk, B. P., Matsuoka, K., Mouginot, J., Nitsche, F. O., Nogi, Y., Nost, O. A., Popov, S. V., Rignot, E., Rippin, D. M., Rivera, A., Roberts, J., Ross, N., Siegert, M. J., Smith, A. M., Steinhage, D., Studinger, M., Sun, B., Tinto, B. K., Welch, B. C., Wilson, D., Young, D. A., Xiangbin, C., and Zirizzotti, A.: Bedmap2: Improved ice bed, surface and thickness datasets for Antarctica, Cryosphere, 7, 375–393, https://doi.org/10.5194/tc-7-375-2013, 2013.

Graham, A. G., Wåhlin, A., Hogan, K. A., Nitsche, F. O., Heywood, K. J., Totten, R. L., Smith, J. A., Hillenbrand, C. D., Simkins, L. M.,

55   Anderson, J. B., Wellner, J. S., and Larter, R. D.: Rapid retreat of Thwaites Glacier in the pre-satellite era, Nature Geoscience, 15, 706–713, https://doi.org/10.1038/s41561-022-01019-9, 2022.

Smith, J. A., Hillenbrand, C.-D., Kuhn, G., Larter, R. D., Graham, A. G., Ehrmann, W., Moreton, S. G., and Forwick, M.: Deglacial history of the West Antarctic Ice Sheet in the western Amundsen Sea Embayment, Quaternary Science Reviews, 30, 488–505, https://doi.org/https://doi.org/10.1016/j.quascirev.2010.11.020, 2011.

60   Smith, J. A., Andersen, T. J., Shortt, M., Gaffney, A. M., Truffer, M., Stanton, T. P., Bindschadler, R., Dutrieux, P., Jenkins, A., Hillenbrand, C. D., Ehrmann, W., Corr, H. F., Farley, N., Crowhurst, S., and Vaughan, D. G.: Sub-ice-shelf sediments record history of twentieth-century retreat of Pine Island Glacier, Nature, 541, 77–80, https://doi.org/10.1038/nature20136, 2017.

Zoet, L. K. and Iverson, N. R.: A slip law for glaciers on deformable beds, Science, 368, https://doi.org/10.1126/science.aaz1183, 2020.